

# The Present and Future Mass of the Milky Way Halo

M.I. Wilkinson and N.W. Evans

*Theoretical Physics, Department of Physics, 1 Keble Road, Oxford, OX1 3NP*

## ABSTRACT

A simple model for the Milky Way halo is presented. It has a flat rotation curve in the inner regions, but the density falls off sharply beyond an outer edge. This truncated, flat rotation curve (TF) model possesses a rich family of simple distribution functions which vary in velocity anisotropy. The model is used to estimate the total mass of the Milky Way halo using the latest data on the motions of satellite galaxies and globular clusters at Galactocentric radii greater than 20 kpc. This comprises a dataset of 27 objects with known distances and radial velocities, of which 6 also possess measured proper motions. Unlike earlier investigations, *we find entirely consistent maximum likelihood solutions unaffected by the presence or absence of Leo I, provided both radial and proper motion data are used*. The availability of the proper motion data for the satellites is crucial as, without them, the mass estimates with and without Leo I are inconsistent at the 99% confidence level. All these results are derived from models in which the velocity normalisation of the halo potential is taken as  $\sim 220 \text{ km s}^{-1}$ .

A detailed analysis of the uncertainties in our estimate is presented, including the effects of the small dataset, possible incompleteness or correlations in the satellite galaxy sample and the measurement errors. The most serious uncertainties come from the size of the dataset, which may cause a systematic underestimate by a factor of two, and the measurement errors, which cause a scatter in the mass of the order of a factor of two. We conclude that the total mass of the halo is  $\sim 1.9_{-1.7}^{+3.6} \times 10^{12} M_{\odot}$ , while the mass within 50 kpc is  $\sim 5.4_{-3.6}^{+0.2} \times 10^{11} M_{\odot}$ . In the near future, ground-based radial velocity surveys of samples of blue horizontal branch (BHB) stars are a valuable way to augment the sparse dataset. A dataset of  $\sim 200$  radial velocities of BHB stars will reduce the uncertainty in the mass estimate to  $\sim 20\%$ . In the coming decade, microarcsecond astrometry will be possible with the *Space Interferometry Mission* (SIM) and the *Global Astrometry Interferometer for Astrophysics* (GAIA) satellites. For example, GAIA can provide the proper motions of the the distant dwarfs like Leo I to within  $\pm 15 \text{ km s}^{-1}$  and the nearer dwarfs like Ursa Minor to within  $\pm 1 \text{ km s}^{-1}$ . This will also allow the total mass of the Milky Way to be found to  $\sim 20\%$ . SIM and GAIA will also provide an accurate estimate of the velocity normalisation of the halo potential at large radii.

**Key words:** Galaxy: fundamental parameters – Galaxy: kinematics and dynamics – Galaxy: halo

## 1 INTRODUCTION

The aim of this paper is to obtain a consistent estimate of the total mass of the Milky Way halo. The structure and extent of the dark matter halos of galaxies is a matter of great strategic importance for modern astrophysics. Of course, it is especially important to extract as much information as possible about the halo of our Galaxy, the proximity of which allows it to be studied in exceptional detail. Unfortunately, the mass and size of the Milky Way halo are amongst the most poorly known of all Galactic parameters. They are much more uncertain than the distance to the Galactic Centre or the Oort's constants, for example.

The Milky Way's gas rotation curve cannot be traced beyond  $\sim 20$  kpc, and so it is natural to look to the kinemat-

ics of stellar tracers of the distant halo for estimates of the mass. The motions of the bound satellites of the Milky Way, together with the globular clusters, contain valuable information about the halo potential in which they are moving. Given a model of the gravity field, it is possible to constrain the values of parameters such as the halo's extent, total mass and velocity anisotropy using the radial velocities and proper motions of the distant satellites and globular clusters. A number of authors have studied this problem (e.g., Little & Tremaine 1987; Zaritsky et al. 1989; Kulessa & Lynden-Bell 1992; Kochanek 1996), obtaining a variety of different mass estimates. One peculiarity of all previous studies, however, is the sensitivity of the mass estimates to whether or not Leo I is bound to the Milky Way. Leo I is unusual in that it has one of the largest radial velocities despite being

the second most distant of the Milky Way satellites. It is evidently desirable to obtain mass estimates which do not depend strongly on the velocity of a single satellite.

The current dataset of satellites and globular clusters at distances greater than 20 kpc from the Galactic Centre contains only 27 objects, of which just 6 have measured proper motions. It has been argued that the dataset on the satellite galaxies is complete (Pryor 1998), though this is perhaps unclear as undiscovered satellites could still be lurking within the Zone of Avoidance, especially at large radii. Even so, simple scaling arguments applied to the volume of the Zone of Avoidance suggest that the number of undiscovered satellites within  $\sim 250$  kpc is  $\lesssim 5$ . The dataset has changed in recent years only through painstaking measurements of the proper motions of some of the closest satellites, such as Ursa Minor and Draco (Scholz & Irwin 1994; Schweitzer, Cudworth & Majewski 1997). However, as there are now real hopes that the next few years will see some substantial progress, it is timely to re-examine the problem in order to determine the avenues along which most progress is liable to be made. First, the *Space Interferometry Mission* or SIM (Unwin, Boden, Shao 1997) offers the possibility of microarcsecond parallaxes and proper motions, albeit with long integration times for objects as faint as the dwarf satellites. Second, the *Global Astrometry Interferometer for Astrophysics* or GAIA (Lindegren & Perryman 1996) will be able to find the space motions of all the satellite galaxies to within 10%, though the distances will be less certain. Third, large samples of blue horizontal branch stars that contaminate quasar surveys are becoming available (Flynn, Sommer-Larsen, Christensen & Hawkins 1995; Warren 1998, private communication; Miller 1998, private communication). These are much more numerous than the satellite galaxies and – even though just their radial velocities and distances will be available – they are an invaluable addition to the dataset.

In Section 2, we present our model of the Milky Way halo and describe its properties in some detail. Our strategy for finding the total mass of the Milky Way halo using the radial velocity and proper motion data for the satellite galaxies and distant globular clusters is also reported. In Sections 3 and 4, we present the results of our analysis of the present dataset. With such a limited amount of data, we must be cautious in interpreting the results of statistical analyses. In order to estimate the amount of uncertainty present in mass estimates, we generate large numbers of synthetic datasets and analyse them in the same way as the real data. Section 5 identifies three main sources of uncertainty – measurement errors, modelling uncertainties and correlations in the dataset – and examines the effect of each in turn to place an error estimate on the mass of the Milky Way. Finally, Section 6 turns to the future and evaluates the best strategies to exploit the expected new information from astrometric satellites and ground-based radial velocity surveys of halo stars.

## 2 THE ALGORITHM

This section is mainly theoretical and discusses in turn our model for the Milky Way halo in Section 2.1 and the tracer population of satellites in Section 2.2. The maximum likelihood algorithm for the mass of the halo is reported in Section 2.3.

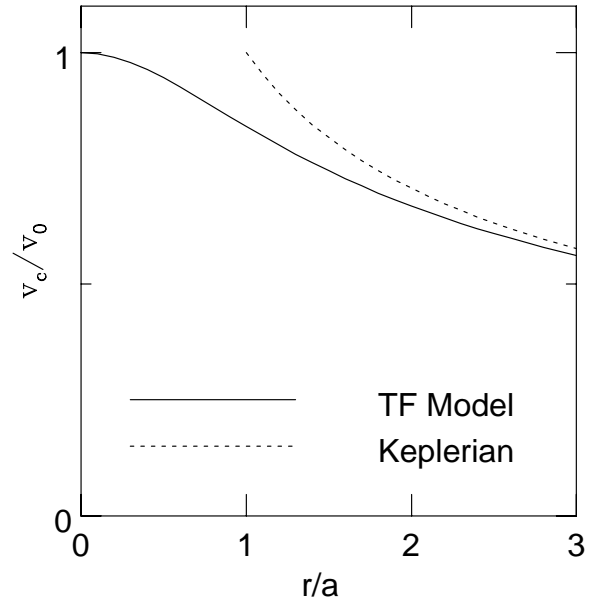


**Figure 1.** Rotation curve of the TF model (solid line) compared with a Keplerian rotation curve (broken line). As  $r \rightarrow \infty$ , the rotation curve of the TF model approaches the Keplerian one.

### 2.1 The Truncated, Flat Rotation Curve (TF) Model

In order to study the dynamical properties of a halo model, it is necessary to know the phase space distribution function (DF). This depends only on the isolating integrals of motion via Jeans (1919) theorem. The isotropic DF depends only on the binding energy per unit mass  $\varepsilon$ . If  $\rho(r)$  is the density of the model and  $\psi(r)$  is the corresponding potential, then the isotropic distribution function is given by the well-known formula (Eddington 1915; Binney & Tremaine 1987)

$$F(\varepsilon) = \frac{1}{\sqrt{8\pi^2}} \frac{d}{d\varepsilon} \int_0^\varepsilon \frac{d\rho}{d\psi} \frac{d\psi}{\sqrt{\varepsilon - \psi}}. \quad (1)$$

This is the simplest possible case, but we can also look for anisotropic DFs which depend on the angular momentum per unit mass  $l$ . A particularly simple and attractive Ansatz is (e.g., Hénon 1973; Dejonghe 1986)

$$F(\varepsilon, l) = l^{-2\beta} f(\varepsilon), \quad (2)$$

where

$$f(\varepsilon) = \frac{2^{\beta-3/2}}{\pi^{3/2} \Gamma[m - 1/2 + \beta] \Gamma[1 - \beta]} \frac{d}{d\varepsilon} \times \int_0^\varepsilon d\psi \frac{d^m r^{2\beta}}{d\psi^m} \rho(\varepsilon - \psi)^{\beta-3/2+m}. \quad (3)$$

Here,  $m$  is an integer whose value is chosen such that the integral in (3) converges. For such a DF, the velocity dispersions  $\langle v_\phi^2 \rangle$  and  $\langle v_\theta^2 \rangle$  are equal, and there is a constant orbital anisotropy  $\beta = 1 - \langle v_\theta^2 \rangle / \langle v_r^2 \rangle$ .

Clearly, the construction of the DF is very much simpler if the density  $\rho$  can be written as an explicit function of the potential  $\psi$ . There are few such simple models known –

although famous ones have been discovered by Jaffe (1983), Hernquist (1990), Evans (1994) and Zhao (1996). We now present another example. This model has a flat rotation curve in the inner regions and at large radii, the density falls off abruptly like  $r^{-5}$ . For this reason, we shall call it the *truncated, flat rotation curve model*, henceforth TF.

The density of the TF model is

$$\rho(r) = \frac{M}{4\pi} \frac{a^2}{r^2(r^2 + a^2)^{3/2}}. \quad (4)$$

and the potential, which can easily be obtained from Poisson's equation, is

$$\psi(r) = \frac{GM}{a} \log\left(\frac{\sqrt{r^2 + a^2} + a}{r}\right). \quad (5)$$

This model is similar to Jaffe's in that the density is cusped like  $r^{-2}$  in the nucleus; it differs in that the density falls off like  $r^{-5}$  rather than like  $r^{-4}$  in the outer reaches. The rotation curve is flat with amplitude  $v_0 = \sqrt{GM/a}$  in the inner parts. The general rule is

$$v_{\text{circ}}^2 = \frac{v_0^2}{(1 + r^2/a^2)^{1/2}}. \quad (6)$$

As Fig. 1 illustrates, the rotation curve becomes Keplerian for  $r \gg a$ . The density can be written in terms of the dimensionless potential  $\phi = \psi/v_0^2$  as

$$\rho(\phi) = \frac{M}{4\pi a^3} \frac{\sinh^5 \phi}{\cosh^3 \phi}. \quad (7)$$

This follows because (5) can be inverted as

$$r(\phi) = a \operatorname{csch} \phi. \quad (8)$$

which is the crucial equation on which the value of the model rests. So, the isotropic DF from equation (1) is

$$F(\varepsilon) = \frac{M}{2\sqrt{2}\pi^3 a^3 v_0^3} \int_0^\varepsilon \frac{d\phi}{(\varepsilon - \phi)^{1/2}} \{ \sinh^2 \phi \tanh \phi + \tanh^3 \phi + 3 \tanh^3 \phi \operatorname{sech}^2 \phi \}. \quad (9)$$

This is not a tractable integral, but the asymptotic behaviour is easily derived. The approximate form of the DF in the envelope ( $\varepsilon \rightarrow 0$ ) is  $F(\varepsilon) \sim \varepsilon^{7/2}$ . Near the central cusp ( $\varepsilon \rightarrow \infty$ ), the DF becomes  $F(\varepsilon) \sim \exp(2\varepsilon)$ .

The velocity dispersions of the isotropic model are

$$\langle v_r^2 \rangle = \langle v_\theta^2 \rangle = \langle v_\phi^2 \rangle = \frac{v_0^2(r^2 + a^2)^{1/2}}{2a^4} \left[ a(2r^2 + a^2) - \frac{2r^2}{a}(r^2 + a^2) \log\left(\frac{r^2 + a^2}{r^2}\right) \right]. \quad (10)$$

A careful Taylor expansion shows that as  $r \rightarrow 0$ ,  $\langle v_r^2 \rangle \rightarrow v_0^2/2$ . The same property is possessed by the Jaffe sphere. This is because the central parts of both models are very similar and resemble the singular isothermal sphere. As  $r \rightarrow \infty$ ,  $\langle v_r^2 \rangle \rightarrow 0$ , as expected. The circular orbit model has  $\langle v_r^2 \rangle = 0$  and  $\langle v_\theta^2 \rangle = \langle v_\phi^2 \rangle = \frac{1}{2}v_{\text{circ}}^2$ . The radial velocity dispersion for a model with constant anisotropy  $\beta = 1 - \langle v_\theta^2 \rangle/\langle v_r^2 \rangle$  is

$$\langle v_r^2 \rangle = \frac{Ma^{2\beta-3}v_0^2}{4\pi r^{2\beta} \rho} \int_0^{\phi(r)} \frac{\sinh^{5-2\beta} \phi}{\cosh^3 \phi} d\phi. \quad (11)$$

The TF potential has been used before by Lin and Lynden-Bell (1982) in their work on the orbits of the Magellanic clouds and by Lynden-Bell & Lynden-Bell (1995) in their

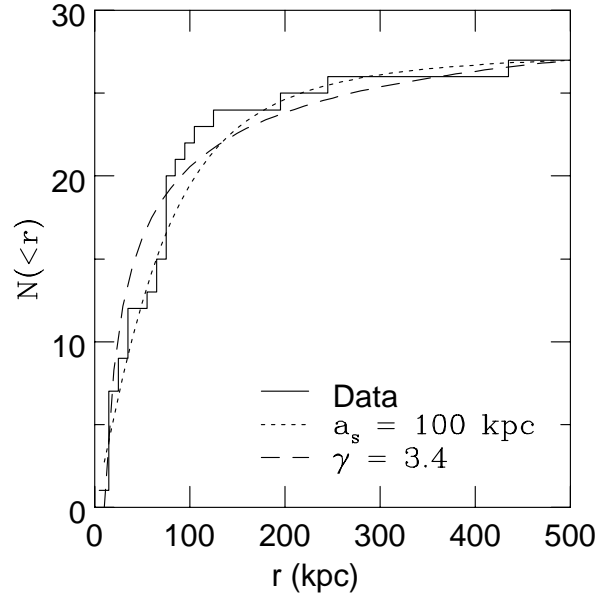


**Figure 2.** The cumulative number  $N(< r)$  of the satellites and distant globular clusters is plotted against Galactocentric radius  $r$ . Superposed are the best fitting shadow (dotted line) and power-law (dashed line) tracer models.

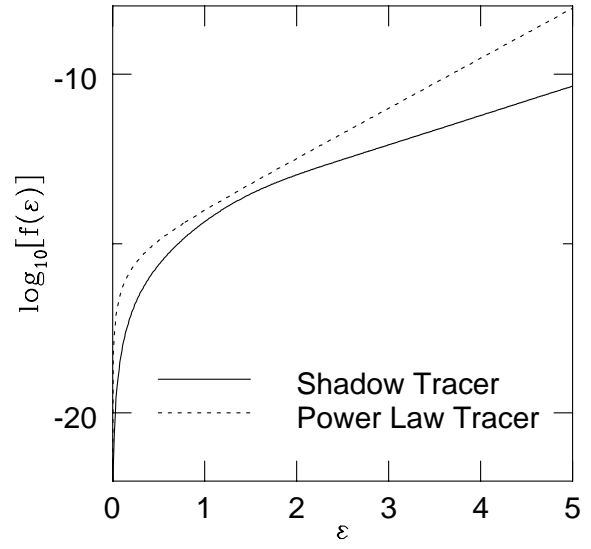


**Figure 3.** Logarithm of the isotropic DF for a shadow tracer model (solid line) compared with that for a power-law tracer model (broken line).

study of the kinematics of halo streams, but its DF does not appear to be available in the literature. In many respects, the TF model rivals the Jaffe sphere in terms of simplicity and usefulness.

## 2.2 The Satellite Number Density

Let us assume that the Milky Way halo is a TF model whose total mass  $M$  is to be found. For the analysis of the distant

**Table 1.** Probability formulae (15) and (16) are given explicitly for the shadow tracer and power-law tracer populations. In each case,  $P(r_i, v_{ri}|a, \beta)$  is the probability when only a radial velocity  $v_{ri}$  is available and  $P(r_i, v_i|a, \beta)$  is the corresponding probability when the full space velocity  $v_i$  is available from proper motion measurements.

Satellite Model	Probability
Shadow Tracer	$P(r_i, v_{ri} a, \beta) = \frac{a_s^2 a^{2\beta-2}}{4\sqrt{2\pi^2 \rho_s r^{2\beta} v_0}} \int_0^{\varepsilon_m} d\phi \frac{[(5-2\beta)a^2 - (2\beta-2)a_s^2 \sinh^2 \phi] \cosh \phi}{(\varepsilon_m - \phi)^{1/2} \sinh^{2\beta-4} \phi (a^2 + a_s^2 \sinh^2 \phi)^{5/2}}$ $P(r_i, v_i a, \beta) = \frac{l^{-2\beta}}{\rho_s} \frac{2^{\beta-5/2} v_0^{2\beta-3} a^{2\beta}}{\pi^{5/2} \Gamma[3/2 + \beta] \Gamma[1 - \beta]} \int_0^{\pi/2} d\theta \sin \theta \cos \theta \frac{d}{d\epsilon} \left[ \epsilon \left( \frac{d^2}{d\phi^2} \left[ \frac{\sinh^{5-2\beta} \phi}{(a^2 + a_s^2 \sinh^2 \phi)^{3/2}} \right] \right) (\epsilon - \phi)^{\beta+1/2} \right]_{\phi \rightarrow \epsilon \sin^2 \theta}$
Power-Law Tracer	$P(r_i, v_{ri} a, \beta) = \frac{a^{2\beta-\gamma} (\gamma-2\beta)}{\sqrt{2\pi r^{2\beta-\gamma} v_0}} \int_0^{\varepsilon_m} d\phi \frac{\sinh^{\gamma-2\beta-1} \phi \cosh \phi}{(\varepsilon_m - \phi)^{1/2}}$ $P(r_i, v_i a, \beta) = \frac{l^{-2\beta} r^{2\beta-1/2} v_0^{2\beta-3} a^{2\beta-\gamma}}{\pi^{3/2} \Gamma[3/2 + \beta] \Gamma[1 - \beta]} \int_0^{\pi/2} d\theta \sin \theta \cos \theta \frac{d}{d\epsilon} \left[ \epsilon \left( \frac{d^2}{d\phi^2} \left[ \sinh^{\gamma-2\beta} \phi \right] \right) (\epsilon - \phi)^{\beta+1/2} \right]_{\phi \rightarrow \epsilon \sin^2 \theta}$

satellites, the most important thing is not the DF of the self-consistent mass density (4) but the DF of a tracer population. For this, we consider two distinct possibilities.

First, the density of the satellites may ‘‘shadow’’ the total density of the halo. In the case of such *shadow tracers*, the number density of the satellites is given by

$$\rho_s(r) \propto \frac{a_s^2}{r^2(r^2 + a_s^2)^{3/2}}. \quad (12)$$

In other words, the satellites follow another TF model with a scalelength  $a_s$  which may or may not be the same as that of the halo. The cumulative number of satellites  $N(< r)$  within radius  $r$  is plotted in Fig. 2. Here, the data are the 27 satellite galaxies and globular clusters at Galactocentric radii greater than 20 kpc. Superposed is the best fitting shadow tracer in dotted lines, for which the scalelength  $a_s$  is 100 kpc. The second alternative is that the number density of the satellites is a scale-free power-law, i.e.,

$$\rho_s(r) \propto \frac{1}{r^\gamma}, \quad (13)$$

where  $\gamma$  is the asymptotic density fall-off. We assume that this law holds good beyond a lower cut-off (to evade the singularity at the origin) and sometimes even an outer cut-off. We shall call this the *power-law tracer* case. The best fitting power-law tracer is also shown in Fig. 2. It has  $\gamma = 3.4$  so that the density indeed falls off like a typical spheroid population.

For the shadow and power-law tracers, the isotropic DF is plotted as a function of binding energy per unit mass in Fig. 3. Anticipating the results in the next Section, the halo is assumed to be a TF model with scalelength  $a = 240$  kpc for the shadow tracer case and  $a = 170$  kpc for the power-law tracer case. In the figure, the shadow tracer population is a TF model with  $a = 100$  kpc and the power-law tracer model has  $\gamma = 3.4$ . More general families of anisotropic DFs (2) are also available as simple quadratures by expressing  $\rho_s(r)$  in terms of the potential using (8) and substituting into (3). We shall not give the formulae here, but proceed to construct the needed probabilities directly.

### 2.3 The Bayesian Likelihood Method

The models contain at least two free parameters, namely  $\beta$  which fixes the anisotropy of the orbits and  $M$  which is the total mass of the Milky Way halo. This section outlines our strategy for constraining the model parameters using the

radial velocities and proper motions of the Milky Way satellites. The method was proposed by Little & Tremaine (1987) and developed further by Kochanek (1996). Of course, the mass  $M$  depends on the scalelength  $a$  through eq. (6), and in what follows all probabilities are quoted in terms of  $\beta$  and  $a$ .

Suppose for each of  $N$  satellites at positions  $r_i$  ( $i = 1 \dots N$ ) we measure the radial velocity  $v_{ri}$ . Given a particular choice of model parameters  $(a, \beta)$ , the probability of finding a satellite at radius  $r_i$  moving with radial velocity  $v_{ri}$  is simply

$$P(r_i, v_{ri}|a, \beta) = \frac{1}{\rho_s} \int d^3 v l^{-2\beta} f(\epsilon) \delta(v_r - v_{ri}). \quad (14)$$

where  $\rho_s$  is the density distribution of the satellites. Using (3) for  $f(\epsilon)$ , it can be shown via Laplace transforms that (e.g., Kochanek 1996)

$$P(r_i, v_{ri}|a, \beta) = \frac{1}{\sqrt{2\pi} \rho_s r^{2\beta}} \int_0^{\varepsilon_m} \frac{d\psi}{(\varepsilon_m - \psi)^{1/2}} \frac{dr^{2\beta} \rho_s}{d\psi}, \quad (15)$$

if  $\varepsilon_m = \psi - v_{ri}^2/2 > 0$  and zero otherwise. Note that this expression holds for all values of  $m$  in equation (3). If we also have the proper motion of a satellite, then we can calculate its total velocity,  $v_i$  and hence its tangential velocity,  $v_{ti} = v_i^2 - v_{ri}^2$ . In this case the delta function in equation (14) becomes  $\delta^3(\mathbf{v} - \mathbf{v}_i)$  and the probability is simply

$$P(r_i, v_i|a, \beta) = \frac{f(\epsilon) l^{-2\beta}}{\rho_s}. \quad (16)$$

if  $\varepsilon = \psi - (v_{ri}^2 + v_{ti}^2)/2 > 0$  and zero otherwise. Table 1 gives the expressions for the probabilities (15) and (16) for each of the two tracer populations.

In order to find the likelihood of a particular set of model parameters given the observations of radial velocities and proper motions, we make use of Bayes’ theorem. This gives us the fundamental formula of the algorithm, namely

$$P(a, \beta|r_i, v_{ri}, I) = \frac{1}{N} P(a) P(\beta|a) \prod_{i=1}^N P(r_i, v_{ri}|a, \beta), \quad (17)$$

where the normalisation  $N$  is given by

$$N = \int da d\beta P(a) P(\beta|a) \prod_{i=1}^N P(r_i, v_{ri}|a, \beta). \quad (18)$$

Here,  $P(a, \beta|r_i, v_{ri}, I)$  is the probability of the model parameters taking the values  $a$  and  $\beta$  given the data  $(r_i, v_{ri})$ .  $I$  denotes the prior information, namely the prior probability distributions,  $P(a)$  and  $P(\beta)$  respectively. We initially chose

**Table 2.** Data on the radial velocities of the satellites and distant globular clusters. The sources are: <sup>a</sup> Harris (1996), <sup>b</sup> Mateo (1998). Listed are Galactic coordinates ( $\ell, b$ ), heliocentric and Galactocentric distances ( $s$  and  $r$ ) in kpc, heliocentric and Galactocentric line of sight radial velocities ( $v_\odot$  and  $v_r$ ) in  $\text{km s}^{-1}$ , together with object type.

Name	$\ell$	$b$	$s$	$r$	$v_\odot$	$v_r$	Type
Pal 13 <sup>a</sup>	87	-43	26	27	-28	138	GC
NGC 5634 <sup>a</sup>	342	49	25	21	-45	-80	GC
NGC 5824 <sup>a</sup>	333	22	31	25	-38	-127	GC
NGC 5694 <sup>a</sup>	331	30	34	28	-146	-232	GC
NGC 6229 <sup>a</sup>	74	40	29	29	-154	22	GC
Pal 15 <sup>a</sup>	19	24	44	37	69	148	GC
NGC 7006 <sup>a</sup>	64	-19	41	38	-378	-180	GC
Pal 14 <sup>a</sup>	29	42	72	67	77	170	GC
Eridanus <sup>a</sup>	218	-41	81	86	-24	-141	GC
NGC 2419 <sup>a</sup>	180	25	82	90	-20	-27	GC
Pal 4 <sup>a</sup>	202	72	100	102	75	51	GC
AM-1 <sup>a</sup>	258	-48	119	120	116	-41	GC
Pal 2 <sup>a</sup>	171	-9	27	35	-133	-105	GC
Arp 2 <sup>a</sup>	9	-21	28	20	115	153	GC
NGC 7492 <sup>a</sup>	53	-63	25	24	-208	-128	GC
Fornax <sup>b</sup>	237	-66	138	140	53	-36	dSph
Leo I <sup>b</sup>	226	49	250	254	286	178	dSph
Leo II <sup>b</sup>	220	67	205	208	76	22	dSph
Sextans <sup>b</sup>	244	42	86	89	227	75	dSph
Phoenix <sup>b</sup>	272	-69	445	445	56	-34	dIrr/dSph
Carina <sup>b</sup>	260	-22	101	103	224	8	dSph

$P(a) \propto 1/a$ , as recommended by Kendall & Stuart (1977) as a suitable prior for a variable that can take values within the range  $(0, \infty)$ . We also experimented with  $P(a) \propto 1/a^2$  as this prior gives lower probabilities for very large (and physically unreasonable) halos. The prior in the velocity anisotropy is taken to be of the general form

$$P(\beta) \propto 1/(3 - 2\beta)^n.$$

When  $n = 0$ , this is a uniform prior. When  $n = 2$ , this corresponds to the prior introduced by Kochanek (1986) in which the ratio of radial kinetic energy to total kinetic energy is uniform. For  $n > 1$ , the ratio of the probability of obtaining a radial  $\beta$  to that of obtaining a tangential  $\beta$  is  $3^{n-1} - 1$ . As  $n \rightarrow \infty$ , the prior becomes increasingly biased towards radial anisotropy. Numerical simulations of halo formation do suggest that halos may well be radially anisotropic (e.g., Dubinski & Carlberg 1991).

### 3 RESULTS

In applying the Bayesian analysis to the observational data, two kinds of calculations suggest themselves. First, the gas

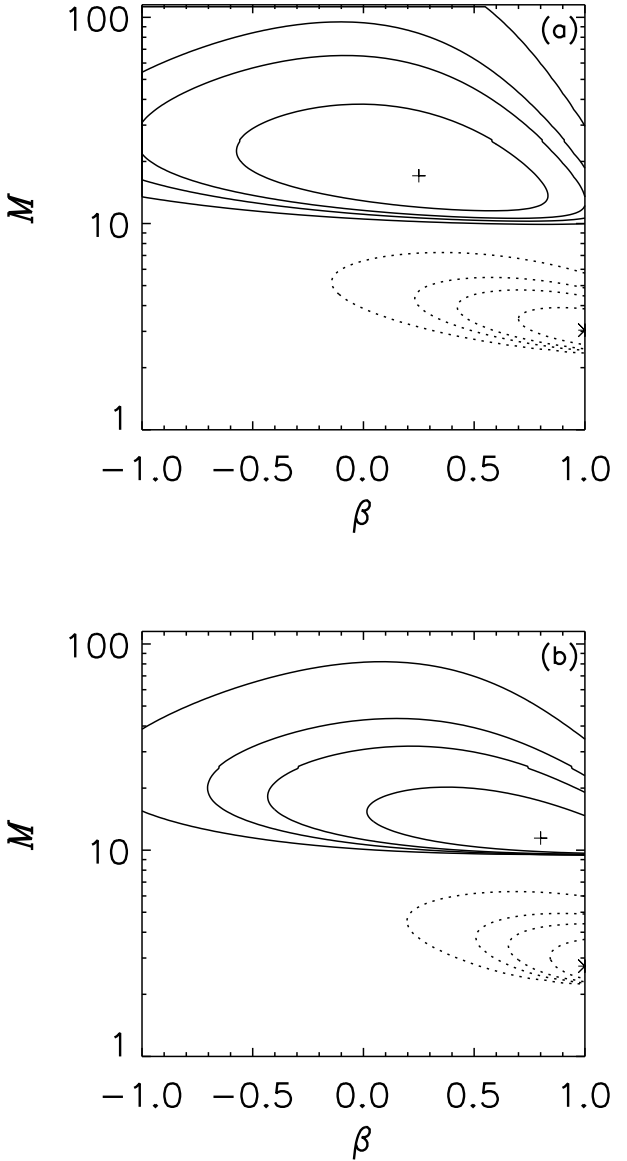


**Figure 4** (a) Likelihood contours for the total mass  $M$  (in units of  $10^{11} M_\odot$ ) and the velocity anisotropy  $\beta$  obtained assuming a shadow tracer satellite population with  $a_s = 100$  and using Milky Way satellite and globular cluster radial velocities only. Results including Leo I (solid curves) and excluding Leo I (dotted curves) are shown. Contours are at heights of 0.32, 0.1, 0.045 and 0.01 of peak height. (b) As in (a) but for the case of a power-law tracer satellite population with  $\gamma = 3.4$ .

rotation curve may be a good guide to the velocity normalisation  $v_0$  in the distant halo. Second, the gravity field in the outer parts of the halo may be very different from the inner parts and so  $v_0$  may be unrelated to the circular velocity near the Sun (c.f. Little & Tremaine 1987). In this Section, the velocity normalisation  $v_0$  is *always* chosen so that the circular speed at the solar radius is  $220 \text{ km s}^{-1}$ . Section 4 studies the implications of allowing  $v_0$  to vary.

**Table 3.** Data on the radial velocities and proper motions of the six satellites for which proper motions are available. All proper motions are quoted as the heliocentric motions  $\mu_\delta$  and  $\mu_\alpha \cos \delta$ , where  $\alpha$  and  $\delta$  are the R.A. and Dec., respectively. All proper motions are in arcsec per century.  $v_r$  and  $v_t$  are the Galactocentric radial and tangential velocities in  $\text{km s}^{-1}$ , calculated assuming  $R_\odot = 8.0$  kpc and the motion of the sun to be (-9, 232, 11) relative to the rest frame of the Galaxy. Sources: 1 - Kroupa & Bastian (1997); 2 - Schweitzer, Cudworth, Majewski, & Suntzeff (1995); 3 - Schweitzer, Cudworth & Majewski (1997); 4 - Odenkirchen, Brosche, Geffert & Tucholke (1997); 5 - Dauphole, Geffert, Colin, Ducourant, Odenkirchen & Tucholke (1996); 6 - Scholz & Irwin (1994); 7 - Mateo (1998). Notes: 1 - The LMC/SMC have been treated as a single object moving with the motion of the LMC but located at the centre of mass of the system. This is justified by noting that Kroupa & Bastian (1997) found that the space motions of the LMC and SMC are roughly parallel; 2 - The value for the Draco proper motion given in Scholz & Irwin (1994) includes the correction for the solar motion.

Name	$\ell$	$b$	$s$	$r$	$v_\odot$	$\mu_\alpha \cos \delta$	$\mu_\delta$	$v_r$	$v_t$	Type	Source
<sup>1</sup> LMC/SMC	282	-34	49	49	274	$0.161 \pm 0.019$	$-0.006 \pm 0.021$	83	249	Irr III-IV	1, 7
Sculptor	288	-83	79	79	108	$0.072 \pm 0.022$	$-0.006 \pm 0.025$	95	202	dSph	2, 7
Ursa Minor	105	45	66	68	-248	$0.022 \pm 0.008$	$0.026 \pm 0.01$	-87	264	dSph	3, 7
NGC4147	253	77	19	21	183	$-0.27 \pm 0.13$	$0.09 \pm 0.13$	222	248	GC	4
Pal 3	240	42	89	93	83	$0.033 \pm 0.023$	$0.030 \pm 0.031$	-65	353	GC	5
<sup>2</sup> Draco	86	35	82	82	-293	$0.09 \pm 0.05$	$0.1 \pm 0.05$	-255	454	dSph	6, 7

### 3.1 The Data on the Satellites

Tables 2 and 3 summarise the data available on satellites and globular clusters at distances greater than 20 kpc from the Galactic Centre, correcting several errors contained in previous presentations of these data – tables of the proper motion data in particular have tended to harbour serious inconsistencies of notation. The radial velocities quoted for the dwarf spheroidals are all based on optical observations except for that of Phoenix which is derived from radio measurements.

In converting the heliocentric quantities to Galactocentric ones, we assume a circular speed of  $220 \text{ km s}^{-1}$  at the Galactocentric radius of the sun ( $R_\odot = 8.0$  kpc) and a solar peculiar velocity of  $(U, V, W) = (-9, 12, 7)$ , where  $U$  is directed outward from the Galactic Centre,  $V$  is positive in the direction of Galactic rotation at the position of the sun, and  $W$  is positive towards the North Galactic Pole. Heliocentric radial velocities are first corrected for solar motion using these values and then adjusted by a factor to take account of contamination of the observed radial velocity by the (unknown) tangential velocity components. This correction is derived from the geometric relationship

$$v_{r\odot} = v_r \cos \alpha + v_t \sin \alpha \cos \psi. \quad (19)$$

Here,  $v_{r\odot}$  is the observed heliocentric radial velocity,  $v_r$  is the Galactocentric radial velocity,  $\alpha$  is the angle between the unit vector  $\hat{\mathbf{r}}$  from the Galactic Centre to the satellite and the unit vector  $\hat{\mathbf{s}}$  from the sun to the satellite, and  $\psi$  is the angle between the normal to the orbital plane and  $\hat{\mathbf{r}} \times \hat{\mathbf{s}}$ . As the DFs depend only on the energy and the modulus of the angular momentum, the velocity ellipsoid is aligned in spherical polar coordinates. By squaring and averaging over the distribution function, we find the (statistical) correction factor is

$$\langle v_r^2 \rangle^{1/2} = \frac{\langle v_{r\odot}^2 \rangle^{1/2}}{\sqrt{1 - \beta \sin^2 \alpha}}, \quad (20)$$

Here, the angled brackets denote ensemble averages, while  $\beta$

is the constant orbital anisotropy. This statistical correction is small for all the satellites in our dataset, even those at Galactocentric radii close to 20 kpc where the offset of the line of sight is greatest.

### 3.2 Results with Radial Velocity Data Only

Let us now apply the methods described in Section 2 to the observational data. In order to emphasise the crucial role played by the proper motions, we first present the results obtained using only the radial velocities of the satellites. Fig. 4(a) shows the likelihood contours in the mass-anisotropy ( $M$ - $\beta$ ) plane for the case of a shadow tracer satellite population with  $a_s = 100$  kpc. The contours obtained when Leo I is assumed to be bound to the Milky Way (solid contours) are very different from those obtained when Leo I is excluded from the dataset (dotted contours). The maximum of the probability surface is shown as a cross (asterisk) for the contours including (excluding) Leo I. When Leo I is included, the most likely value of the total halo mass  $M$  is  $17.0 \times 10^{11} M_\odot$  corresponding to a scalelength  $a$  of 150 kpc for the halo. When Leo I is excluded, the most likely values of  $M$  and  $a$  shrink to  $3.0 \times 10^{11} M_\odot$  and 25 kpc respectively. The contours in Fig. 4(a) are obtained using  $1/a^2$  as the prior probability on  $a$  and the uniform energy prior ( $n = 2$ ) on  $\beta$ . Fig. 4(b) shows the contours obtained using the same priors but for a power-law tracer satellite population with  $\gamma = 3.4$ . In this case, the most likely value of  $M$  is  $11.4 \times 10^{11} M_\odot$  ( $a = 100$  kpc) if Leo I is included and  $2.7 \times 10^{11} M_\odot$  ( $a = 25$  kpc) if Leo I is excluded. For both shadow and power-law tracer populations, we conclude that if we use only radial velocities to estimate the total mass of the Milky Way halo, then the dominant uncertainty is whether or not Leo I is bound.

Table 4 summarises the results obtained for both shadow tracers and power-law tracers using a variety of different priors on  $a$  and  $\beta$ . This table also illustrates the effect of varying the assumed value of  $a_s$  for a shadow tracer population and  $\gamma$  for a power law tracer population. There are

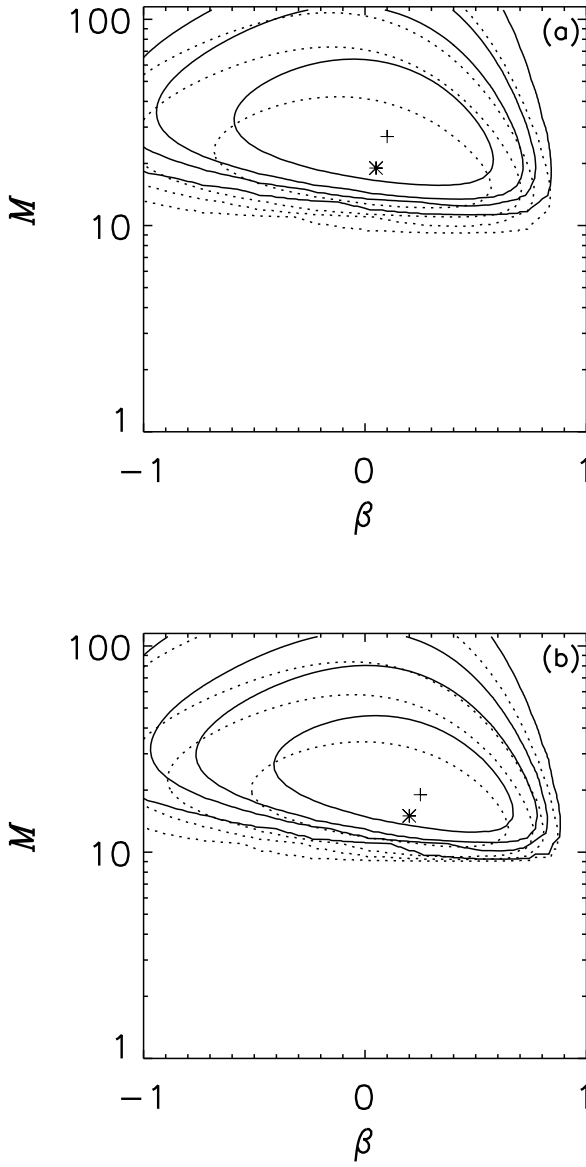


**Figure 5** (a) Likelihood contours for the mass  $M$  (in units of  $10^{11} M_\odot$ ) and the velocity anisotropy  $\beta$  obtained assuming a shadow tracer satellite population with  $a_s = 100$  and using Milky Way satellite and globular cluster radial velocities and proper motions. Results including Leo I (solid curves) and excluding Leo I (dotted curves) are shown. Contours are at heights of 0.32, 0.1, 0.045 and 0.01 of peak height. (b) As in (a) but for the case of a power-law tracer satellite population with  $\gamma = 3.4$ .

a number of trends visible in the results of Table 4. We observe that for the shadow tracers, changing the prior on  $a$  from  $1/a$  to  $1/a^2$  leads to a decrease in the estimate of the total mass. This is natural, since by choosing the  $1/a^2$  prior we are forcing the halo to be smaller. Exactly the same effect is observed for the power-law tracers. Changing the prior on  $a$ , however, has the desirable effect of reducing the size of the likelihood contours in the  $(M, \beta)$  plane. This has a sound physical basis, as the Milky Way halo cannot extend to Megaparsec scales (see e.g., Evans (1997), Gates, Kamionkowski & Turner (1997), as well as Cowsik, Ratnam

& Bhattacharjee (1996) for a heterodox viewpoint). Switching the prior on  $\beta$  from the uniform energy prior ( $n = 2$ ) to a uniform prior ( $n = 0$ ) leads to an increase in the mass estimates including Leo I. This may be understood by noting that the uniform energy prior is biased towards radially anisotropic velocity distributions. A uniform prior gives comparatively more weight to tangential distributions in which the satellites have large (unknown) tangential velocities. This, naturally, implies a larger total halo mass.

Table 4 also shows that our choice of  $a_s$  for the shadow tracers does not have a significant effect on the mass estimate. If, instead of using  $a_s = 100$  kpc, we assume that the satellite scalelength is the same as that of the halo, the mass estimate both with and without Leo I are changed by less than 30 %. For the power-law tracers, increasing the value of the power index  $\gamma$  leads to an increase in the mass estimate. This may be understood in terms of the likelihood of obtaining a distant satellite in a power-law density model. As  $\gamma$  increases, the satellite density falls off faster, making distant satellites less common. In order to fit the observed data which contains distant satellites, the halo must necessarily be larger.

### 3.3 Results with Radial and Proper Motion Data

Having considered the radial velocity data in isolation, we now include the available proper motions in our analysis. In the past few years, the number of measured proper motions of distant clusters and satellites has doubled and the accuracy of these measurements has improved. More importantly, the future holds the prospect of rapid progress using space-based astrometric satellites. At present, the proper motion errors are still large and so we must take account of them. This is done by convolving the probabilities given in Section 2 with an error function to obtain the probability  $P(r_i, v_{i,obs}|a, \beta)$  of obtaining the observed full-space velocity  $v_{i,obs}$  given the values of the model parameters. Thus we obtain

$$P(r_i, v_{i,obs}|a, \beta) = \int \int dv_\alpha dv_\delta E_1(v_\alpha) E_1(v_\delta) \times P(r_i, v_i(v_\odot, v_\alpha, v_\delta)|a, \beta), \quad (21)$$

where  $v_\alpha$  and  $v_\delta$  are the velocities perpendicular to the line of sight and  $v_\odot$  is the radial velocity. The error convolution function  $E_1(v_\alpha)$  is the probability of obtaining the observations given the true velocity  $v_\alpha$  and the estimates of the associated errors. It is likely that the observational errors are strongly non-Gaussian. We assume the Lorentzian error convolution function  $E_1$  given by

$$E_1(v) = \frac{1}{\sqrt{2\pi}\sigma_1} \frac{2\sigma_1^2}{2\sigma_1^2 + (v - v_{obs})^2}. \quad (22)$$

Lorentzians have broader wings than the more familiar Gaussians. In fact,  $E_1(v)$  is the first member of a sequence of error convolution functions which gradually tend towards Gaussianity. As this family of functions may find further applications in astronomy, their properties are presented in more detail in Appendix A. Here, we note only that in order to normalise  $E_1$ , we choose  $\sigma_1$  such that the quartiles of  $E_1$  are the same as those of a Gaussian of width  $\sigma_G$ , where  $\sigma_G$  is the published error estimate. We obtain the relation

$$\sigma_1 = 0.477\sigma_G \quad (23)$$

**Table 4.** Mass estimates obtained using Bayesian analysis applied to the radial velocity data only. All masses are in units of  $10^{11} M_{\odot}$  and all lengths are in kpc.

$a_s$	$a$ prior	$\beta$ prior	Shadow		Tracers		$M(< 50)$	$M(< 100)$
			Most likely $\beta$	Most likely $a$	Most likely $M_{tot}$			
100	$1/a^2$	Energy	With Leo I	0.25	150	17.0	5.3	9.4
			Without Leo I	1.0	25	3.0	2.6	2.9
100	$1/a$	Energy	With Leo I	0.15	180	20.5	5.4	9.8
			Without Leo I	1.0	25	3.0	2.6	2.9
100	$1/a^2$	Uniform	With Leo I	-0.1	175	19.5	5.4	9.8
			Without Leo I	0.95	25	3.0	2.6	2.9
$a_{\text{halo}}$	$1/a^2$	Energy	With Leo I	0.2	135	15.0	5.3	9.1
			Without Leo I	1.0	36	4.1	3.4	3.9
			Power-Law		Tracers			
$\gamma$	$a$ prior	$\beta$ prior	Most likely $\beta$		Most likely $a$	Most likely $M_{tot}$	$M(< 50)$	
			With Leo I	0.8	100	11.4	5.0	8.0
3.4	$1/a^2$	Energy	Without Leo I	1.0	23	2.7	2.5	2.7
			With Leo I	0.75	105	12.0	5.1	8.2
3.4	$1/a$	Energy	Without Leo I	1.0	24	2.8	2.6	2.8
			With Leo I	0.35	120	13.5	5.2	8.7
3.4	$1/a^2$	Uniform	Without Leo I	1.0	23	2.7	2.5	2.7
			With Leo I	1.0	105	12.0	5.1	8.2
4	$1/a^2$	Energy	Without Leo I	1.0	28	3.3	2.9	3.2

**Table 5.** Mass estimates obtained using Bayesian analysis applied to the radial velocity and proper motion data, assuming a Lorentzian error convolution function for the observational errors on the proper motions. All masses are in units of  $10^{11} M_{\odot}$  and all lengths are in kpc.

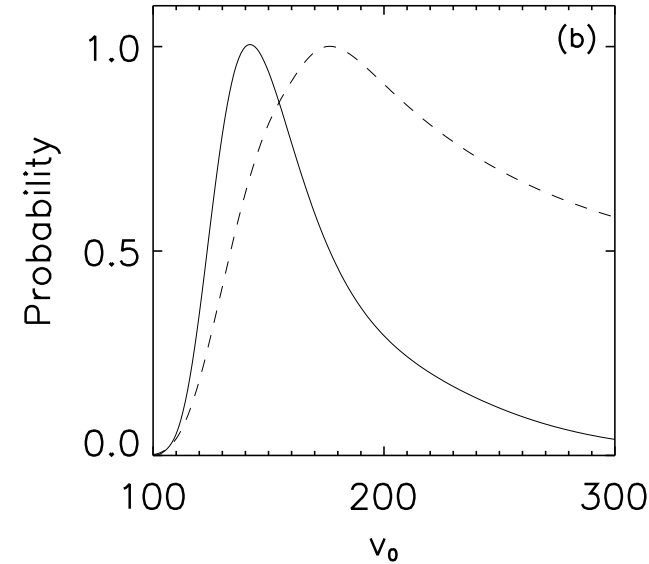
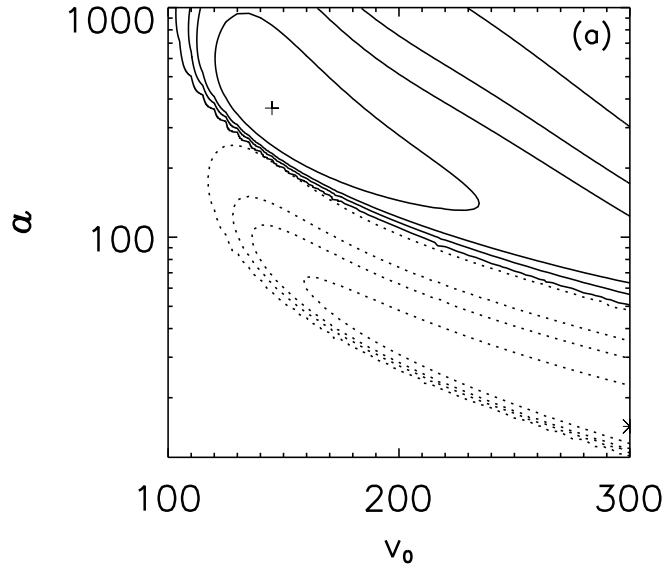
$a_s$	$a$ prior	$\beta$ prior	Shadow		Tracers		$M(< 50)$	$M(< 100)$
			Most likely $\beta$	Most likely $a$	Most likely $M_{tot}$			
100	$1/a^2$	Energy	With Leo I	0.1	240	27.0	5.5	10.4
			Without Leo I	0.05	170	19.0	5.4	9.7
100	$1/a$	Energy	With Leo I	0.05	295	33.0	5.5	10.7
			Without Leo I	0.0	205	23.0	5.5	10.1
100	$1/a^2$	Uniform	With Leo I	-0.15	260	29.0	5.5	10.4
			Without Leo I	-0.2	185	21.0	5.4	9.9
$a_{\text{halo}}$	$1/a^2$	Energy	With Leo I	-0.15	240	27.0	5.5	10.4
			Without Leo I	-0.1	170	19.0	5.4	9.6
			Power-Law		Tracers			
$\gamma$	$a$ prior	$\beta$ prior	Most likely $\beta$		Most likely $a$	Most likely $M_{tot}$	$M(< 50)$	
			With Leo I	0.25	170	19.0	5.4	9.6
3.4	$1/a^2$	Energy	Without Leo I	0.2	135	15.0	5.3	9.1
			With Leo I	0.15	225	25.0	5.5	10.3
3.4	$1/a$	Energy	Without Leo I	0.1	170	19.0	5.4	9.6
			With Leo I	0.0	205	23.0	5.5	10.1
3.4	$1/a^2$	Uniform	Without Leo I	-0.05	150	17.0	5.3	9.1
			With Leo I	0.3	205	23.0	5.5	10.1
4	$1/a^2$	Energy	Without Leo I	0.3	150	17.0	5.3	9.1

and use this in all the convolutions. In what follows we neglect the errors in the heliocentric radial velocities and distances of the satellites, as initial tests indicated that their effect is negligible compared to that of the proper motions.

Fig. 5 shows the likelihood contours obtained by the above procedure for our standard shadow tracer and power-

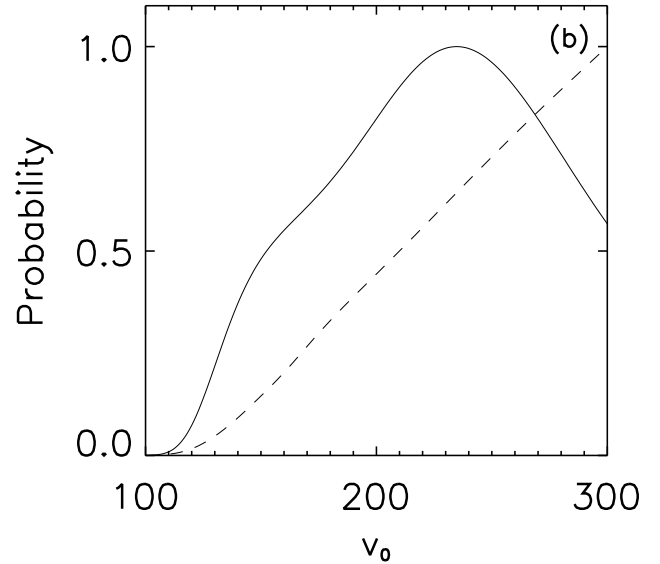
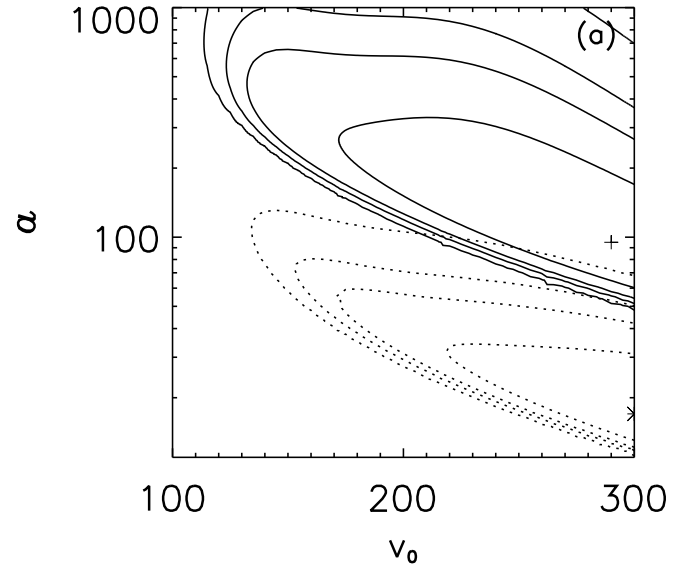
law tracer models. *There is good agreement between the contours based on datasets with and without Leo I.* This removes a longstanding impasse in the subject (c.f., Little & Tremaine 1987; Kulessa & Lynden-Bell 1992; Kochanek 1996).

Table 5 summarises the results obtained when the



**Figure 6.** Likelihood contours for the scale-length  $a$  (in kpc) and the velocity normalisation  $v_0$  obtained assuming a shadow tracer satellite population with  $a_s = 100$  and using Milky Way satellite and globular cluster radial velocities only. Results including Leo I (solid curves) and excluding Leo I (dotted curves) are shown. Contours are at heights of 0.32, 0.1, 0.045 and 0.01 of peak height. Also shown is the marginal distribution for the velocity normalisation. The contours are generated assuming the uniform energy prior probability for  $\beta$  and a  $1/v_0^2$  prior on  $v_0$ .

proper motions of the satellites are included. It can be compared directly with Table 4 obtained for the same models and priors. As before, changing the  $a$  prior from  $1/a$  to  $1/a^2$  leads to a decrease in the mass estimate. Changing the assumed value of  $a_s$  for the shadow tracer population leaves the mass estimate unchanged, although  $\beta$  moves towards more tangential velocity distributions. Increasing the value of  $\gamma$  for the power-law tracers increases the mass estimates



**Figure 7.** As Fig. 6, but the contours are generated assuming uniform prior probabilities for both  $\beta$  and  $v_0$ .

both with and without Leo I by  $\lesssim 20\%$ .

To determine our best estimates for the mass, we compare the area of overlap of the contours with and without Leo I for each of the models in Table 5 and calculate the fractional change in the mass estimate when Leo I is removed. This area is maximised and the fractional change minimised when the total mass of the halo is  $2.7 \times 10^{12} M_\odot$  assuming a shadow tracer population with scalelength 100 kpc, and  $1.9 \times 10^{12} M_\odot$  assuming a power-law tracer population with  $\gamma = 3.4$ . These two mass estimates are in reasonably good agreement, in that the estimate obtained from the power-law tracers lies comfortably within the 32% contour for the shadow tracers and vice versa. The power-law tracer result is more insensitive to the presence of Leo I and we therefore

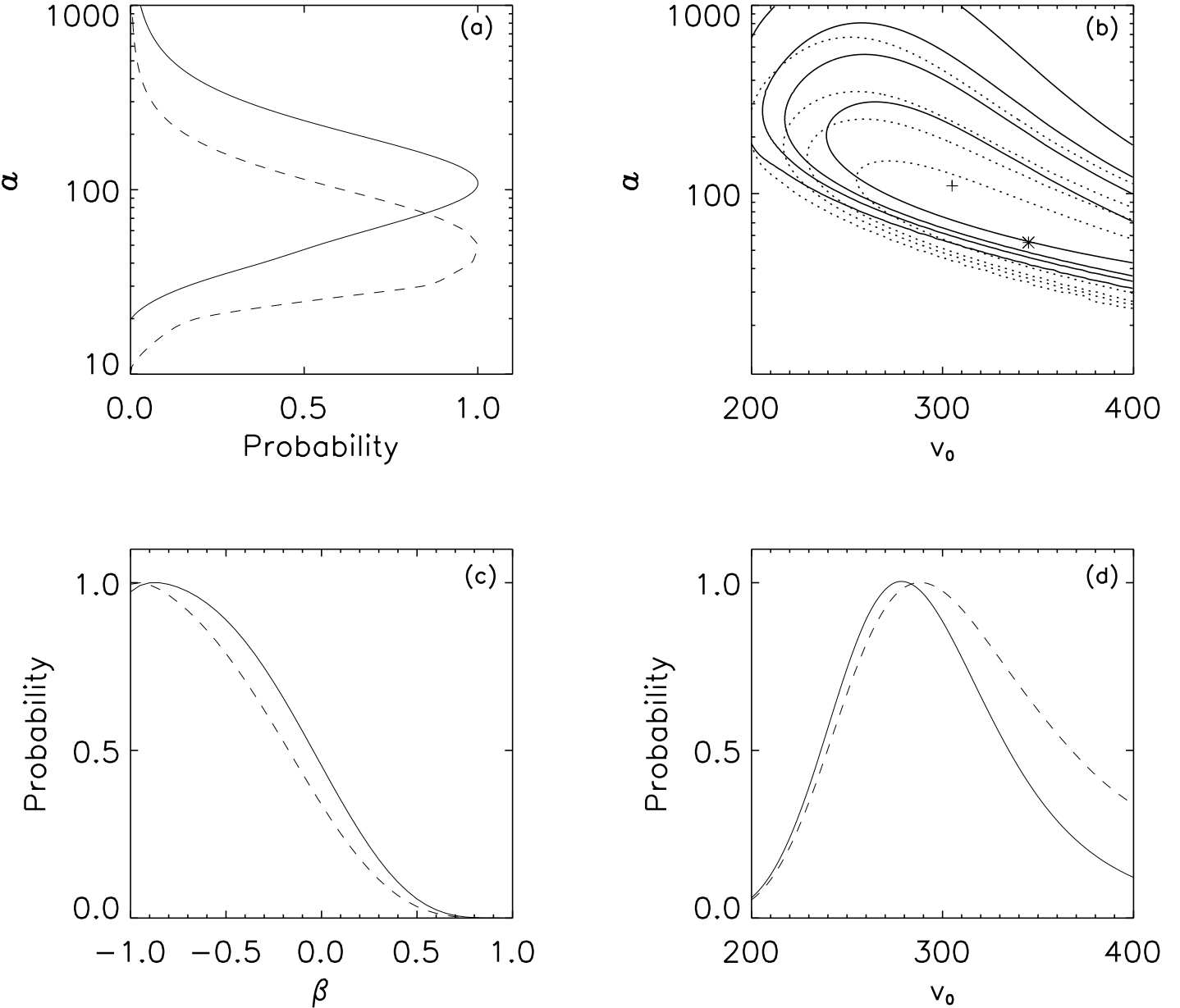


**Figure 8.** Likelihood contours for the scale-length  $a$  (in kpc) and the velocity normalisation  $v_0$  (in km s<sup>-1</sup>) obtained assuming a shadow tracer satellite population with  $a_s = 100$  and using Milky Way satellite and globular cluster radial velocities and proper motions. Results including Leo I (solid curves) and excluding Leo I (dotted curves) are shown. Contours are at heights of 0.32, 0.1, 0.045 and 0.01 of peak height. Also shown are the marginal distributions for the three parameters, including the velocity anisotropy  $\beta$ .

conclude that it is (marginally) the more satisfactory of the two. The 32% contours in Fig. 5(b) give a range of  $1.5 - 4.8 \times 10^{12} M_\odot$  for the power-law estimate. As we shall see in Section 5, this range is in fact an underestimate of the true uncertainty.

It is interesting at this point to ask how likely it is that a single satellite in a dataset of 30 objects with radial velocities drawn randomly from our TF halo model would make a substantial difference to the mass estimate. We generate 1000 datasets and obtain the likelihood contours with the full dataset and minus each of the satellites in turn. We find

that approximately 0.3% of datasets contain a satellite for which the mass estimates with and without the satellite differ by more than a factor of five (c.f. Fich & Tremaine 1991). This result varies from 0.1 – 0.5% as  $\beta$  is varied from 0.9 to –9.0. Thus, Leo I is a rather unusual object and our prior expectation is not to find such a satellite. In the simulations, the data are generated consistently from the model, but it is nonetheless the case that removing one data point from the radial velocity dataset can very occasionally cause a large shift in the likelihood contours in the Bayesian analysis.

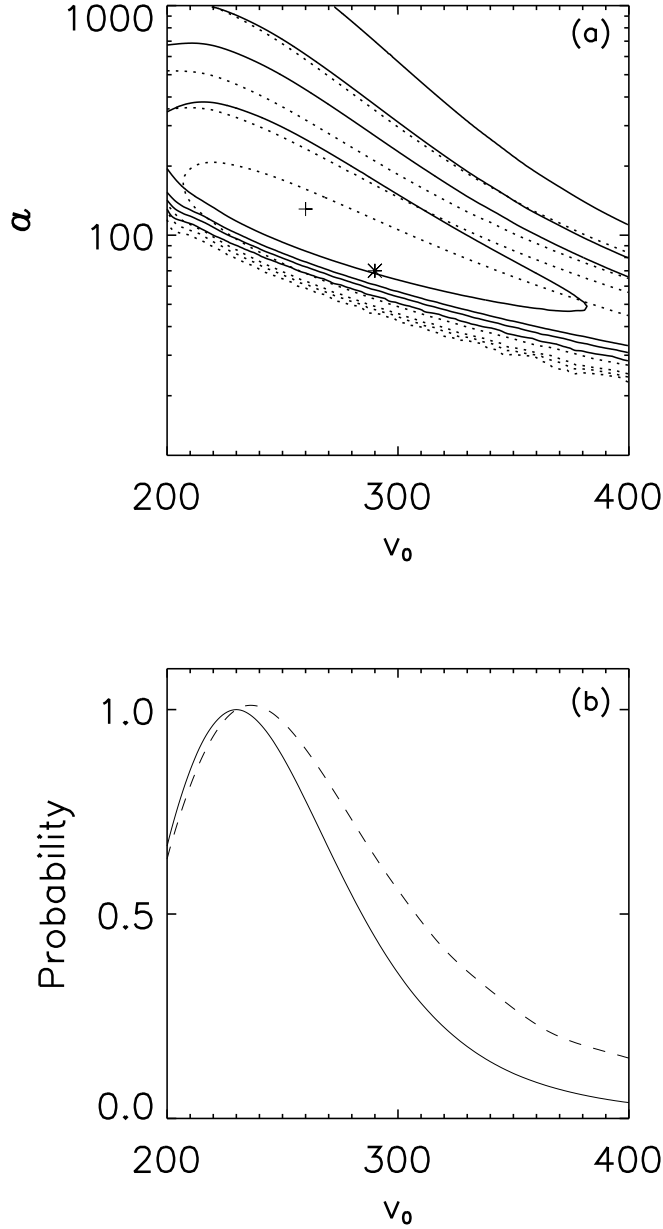


**Figure 9.** Likelihood contours for the scale-length  $a$  (in kpc) and the velocity normalisation  $v_0$  obtained assuming a shadow tracer satellite population with  $a_s = 100$  and using Milky Way satellite and globular cluster radial velocities and proper motions. Results including Leo I (solid curves) and excluding Leo I (dotted curves) are shown. Contours are at heights of 0.32, 0.1, 0.045 and 0.01 of peak height. Also shown is the marginal distribution for the velocity normalisation. The contours were generated assuming a prior probability for  $\beta$  which is strongly biased towards radial anisotropy (see text for discussion).

#### 4 THE VELOCITY NORMALISATION

Thus far, our analysis has assumed that the normalisation  $v_0$  of our halo model is fixed by the constraint that the rotation curve has an amplitude of  $\sim 220 \text{ km s}^{-1}$  at the Sun. We

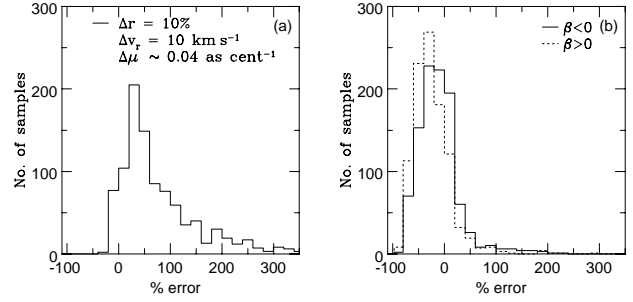


**Figure 10.** (a) Histogram showing the effects of present-day measurement errors on the mass estimate obtained. (b) Histograms illustrating the effects of streams in the data, when all 30 data-points lie on either of two streams. In both cases, the histograms show the number out of 1000 datasets yielding a given percentage error in the mass estimate  $M$ .

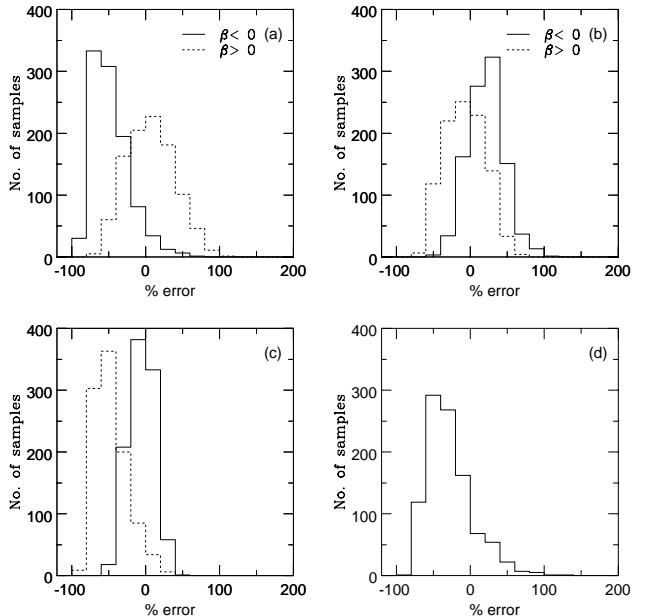


**Figure 11.** Histograms to illustrate the effects of various modelling uncertainties on the mass estimate. All histograms show the number of datasets out of 1000 which yielded a given percentage error in  $M$ . (a) Datasets of 30 points using only radial velocities – lack of knowledge about  $\beta$  gives uncertainty in mass (b) As in (a) but with proper motions included. (c) Datasets of 30 points generated using a TF model with  $a_s = 100$  kpc but with a power-law model (with  $\gamma = 4.0$ ) used in the Bayesian analysis. Two cases are shown, with (solid curve) and without (dashed curve) proper motion data. (d) Datasets of 30 radial velocities where the velocity normalisation is allowed to be a free parameter in the algorithm. The uncertainty in  $M$  is not significantly increased above that in Fig. 12(a) in which  $v_0$  is assumed known.

regard this as an economical assumption to make. For example, if an isotropic tracer population has a density falling off like  $\rho \sim r^{-3}$  in a galaxy with a flat rotation curve of amplitude  $v_0$ , then (Lynden-Bell & Frenk 1981, Evans, Häfner & de Zeeuw 1997)

$$v_0^2 = 3\langle v_r^2 \rangle.$$

Using the data in Table 2 and 3, this gives  $v_0 = 220 \text{ km s}^{-1}$  almost exactly – in good agreement with our assumption. Nonetheless, it is clearly interesting to relax this condition, especially as visible matter dominates the gravity field at the solar radius whilst the dwarf satellites are in the region where dark matter dominates. As Little & Tremaine (1987) first pointed out, the fact that rotation curves at radii between 5 and 20 kpc indicate a logarithmic potential, and that satellite galaxies at 100 kpc indicate a logarithmic potential, does not imply that the circular speeds in the two potentials are precisely the same. So, this section presents results when the Bayesian analysis is performed in the three dimensional parameter space of  $a$ ,  $\beta$  and  $v_0$ . The required probabilities are easily obtained by a straightforward extension of the formulae in Section 2.

Fig. 6 (a) presents contours in the  $(a, v_0)$  plane for a shadow tracer model when only the radial velocities of the satellites are used. In generating this figure, a prior probability of  $1/v_0^2$  was assumed for  $v_0$  and the uniform energy ( $n = 2$ ) prior was used for  $\beta$ . As in Fig. 4 (a) the contours with and without Leo I are disjoint at the 99% level. The marginal distributions of Fig. 6 (b) show that the most likely values of  $v_0$  are  $140 \text{ km s}^{-1}$  including Leo I and  $175 \text{ km s}^{-1}$  excluding Leo I. We also find that  $\beta \sim 1$  both with and without Leo I. This seems in accord with the earlier results of Little & Tremaine (1987), who estimated  $v_0 \lesssim 165 \text{ km s}^{-1}$  using a smaller sample of ten objects together with an infinite isothermal sphere model. The situation changes dramatically, however, if we change the prior probabilities used in the Bayesian analysis. Fig. 7 presents the likelihood contours and marginal distributions for  $v_0$  when the priors on  $v_0$  and  $\beta$  are now uniform. As the figure clearly shows, the most likely values for  $v_0$  are now  $235 \text{ km s}^{-1}$  with Leo I and  $> 300 \text{ km s}^{-1}$  without. This strong sensitivity to the choice of priors is a cause for alarm, and suggests that none of the values of the velocity normalisation are firmly established. Let us also remark that the likelihood curves in the plane of  $(M, \beta)$  with and without Leo I always remain disjoint. In fact, if we simply adjust the value of the velocity normalisation with the aim of obtaining overlapping contours in the  $(M, \beta)$  plane, we are driven towards extremely low values of  $v_0$  ( $\sim 80 \text{ km s}^{-1}$ ) and unphysically large values of the scalelength  $a$  ( $\sim 1 \text{ Mpc}$ ). This is simply because reducing the value of  $v_0$  means that a larger halo scalelength is required to ensure that all the satellites are bound – for large scalelengths, Leo I is buried deep within the halo and therefore has a less significant effect on the total mass.

We now proceed to include the proper motion data to see if the situation is improved. Fig. 8 (b) presents contours in the  $(a, v_0)$  plane for a shadow tracer model when the proper motion data are included, together with the marginal distributions for the three model parameters. We note first that the most likely values of  $a$  and  $v_0$  yield a mass estimate of  $2.4 \times 10^{12} \text{ M}_\odot$  with Leo I and  $1.7 \times 10^{12} \text{ M}_\odot$  without Leo I. This is in broad agreement with the results of Section 3. However, it is clear that the details of the results in Fig. 8 are significantly different. In particular, the anisotropy parameter now has a most likely value of  $-0.95$ , indicating a strongly tangential velocity distribution. Perhaps more significantly, the marginal distributions in Fig. 8 indicate that most likely value for the velocity normalisation is  $\sim 280 \text{ km s}^{-1}$ , irrespective of whether Leo I is included

or excluded. Our high result for the velocity normalisation is an inevitable consequence of the tangential anisotropy of the subsample of 6 satellites with proper motions, which already have  $\beta \sim -1$ . The greater the tangential anisotropy, the larger the normalisation of the halo required to confine the satellites. There are worries about the credibility of this velocity normalisation, as the subsample of satellite galaxies with proper motions may suffer from selection effects. First, it is evidently easier to measure the proper motions for the closer satellites. If the velocity anisotropy changes in a systematic way – for example, if it becomes more radially anisotropic with radius – then the closer satellites will not be representative. Second, the large errors in some of the present proper motions mean that even the direction of the proper motions is sometimes in doubt as the error exceeds the absolute value of the measurement. For example, in the case of Sculptor, the best value of  $\mu_\delta$  is nearly zero, but the large error can produce velocities in either direction. Obviously, these will bias our result towards tangential anisotropy and higher velocity normalisation. A third selection effect is the way in which the objects for which we currently have proper motion data were chosen. As described in Majewski & Cudworth (1993), astrometric projects to measure proper motions are currently “at the mercy of the interests of earlier observers” as this determines whether or not sufficient past epoch plate material exists for comparison with present epoch plates. This represents a bias which is almost impossible to model.

More worryingly, Fig. 9 shows the effects of changing the prior on the velocity anisotropy. Here, we have chosen the  $n = 10$  case in (19) which means that there is a rather significant bias towards radial anisotropy. The upper panel again shows the likelihood contours in the  $(a, v_0)$  plane, whilst the lower panel shows the marginal distribution for  $v_0$ . The maxima of the marginal distributions occurs at  $v_0 = 230 \text{ km s}^{-1}$  and at  $\beta = 0.5$ . Thus by varying the assumed prior on  $\beta$ , our best estimates for  $v_0$  can change very considerably, even when the proper motion data are included. Strong sensitivity to the choice of prior probabilities is a sign that we are trying to extract too much information from the available data and we therefore conclude that given the current dataset it is not realistic to constrain the velocity normalisation of our model from the satellite data alone. More optimistically, we will show in Section 6 that the forthcoming space-borne astrometry satellites SIM and GAIA will be able to put tight constraints on the value of  $v_0$ .

## 5 ERROR ANALYSIS

This section considers three sources of error – namely, measurement errors, uncertainties caused by correlations and streaming in the satellite galaxies and uncertainties due to the modelling itself. The fourth major source of uncertainty is that due to the small size of the dataset – this will be considered in Section 6. We use Monte Carlo simulations to estimate the importance of each effect. We generate artificial datasets of positions and velocities drawn from DFs with  $a$ ,  $v_0$  and  $\beta$  fixed. The algorithm of Section 2 is then applied to see which values of the model parameters are recovered, and hence the likely uncertainty caused by the error source. In most cases, the value of  $v_0$  is fixed in the Bayesian analysis so that the circular speed at the radius of the Sun is  $220$

$\text{km s}^{-1}$ . However, when we consider modeling uncertainties in Section 5.3, we present the effect of allowing  $v_0$  to vary in the analysis. For each type of uncertainty, this procedure is carried out for 1000 datasets. Let us note that in generating the artificial satellites, we approximate the anisotropic DFs by Gaussians whose widths are given by the velocity dispersions. Such approximate DFs can very occasionally generate objects which are not bound to the Milky Way. We test for this in each dataset and discard any object that is unbound. Our approximate DFs still slightly overestimate the number of weakly bound objects, and this leads to a slight but systematic overestimate of the mass. This effect can be observed by careful scrutiny of some of the histograms presented below (for example, in Fig. 12 (a)). Let us emphasise that this systematic error is always much smaller than the errors caused by the effects we are investigating in this section. In what follows, we always quote uncertainties in terms of the average absolute deviation about the mean rather than the standard deviation. This is the preferred way of reporting errors in cases where the distribution is broad (see e.g., Press, Teukolsky, Vetterling & Flannery 1992).

### 5.1 Measurement Errors

The typical errors in the radial velocity measurements are  $\pm 10 \text{ km s}^{-1}$  while those in the heliocentric distances are  $\sim 10\%$ . To determine the importance of these errors for a dataset containing 30 points, we generate an artificial dataset containing 30 data points with both radial velocities and proper motions. To simulate crudely the selection effects in measuring proper motions, we keep only the largest proper motions, which leaves us with 9 proper motions for the case illustrated in Fig. 10 (a). We analyse this dataset to obtain a mass estimate. Fig. 10(a) shows the spread in mass estimates obtained from 1000 further realisations of the same dataset generated by drawing points from Gaussian distributions centred on the data points and with widths representing the measurement uncertainties. The assumed errors are 10% in the distances and  $\pm 10 \text{ km s}^{-1}$  in the radial velocity and  $\pm 40 \mu\text{as yr}^{-1}$  in the proper motions. For these values,  $\sim 30\%$  of mass estimates lie more than a factor of two above the value that would be reported in the absence of measurement errors. The average absolute deviation of the estimates about the mean value is 90% of  $M$ , indicating a very large spread. We conclude that *at present measurement errors are a serious source of uncertainty in our mass estimate, with the proper motion errors dominating, giving rise to slightly more than a factor of 2 uncertainty.*

### 5.2 Correlations in the Dataset

The use of a Bayesian statistical argument implicitly assumes that the data constitute a random sampling of the underlying distribution. As has been known for some time, a number of the satellites of the Milky Way appear to lie on one of two great circles (see for example Lynden-Bell 1976, Kunkel & Demers 1976, Fusi Pecci, Bellazzini, Cacciari & Ferraro 1995). If the satellites are in fact the remains of larger galaxies which have been torn apart by the tidal forces of the Milky Way, then their motions will necessarily be highly correlated. This will reduce the amount of information contained in the dataset of satellite positions and

velocities (although see Johnston, Zhao, Spergel & Hernquist (1999) for a possible application of streams for mass estimates).

To determine whether streams or moving groups of satellites have a significant effect on our analysis, we generate datasets in the (somewhat extreme) case in which the satellites are dispersed onto two streams. Each dataset contains 30 data points and we assume that the full space velocities of all 30 points are known. The results are presented in Fig. 10 (b) for halo models with both radially and tangentially anisotropic velocity distributions. If the satellite galaxies do lie on streams, then this causes a systematic underestimate in both the halo length scale  $a$  and the mass  $M$ . The effect is less significant – but still present – when the velocity dispersion tensor is tangential ( $\beta < 0$ ) as opposed to radial ( $\beta > 0$ ). The underestimate in the mass is of order 20–50%. The average deviation in the mass estimates about the mean value is 26% of  $M$  for  $\beta > 0$  and 29% for  $\beta < 0$ . As a result, we conclude that this source of error is almost certainly not so serious for our dataset as that caused by measurement errors.

### 5.3 Modelling Uncertainties

A third major problem arises from our use of parametric fitting – there is of course no guarantee that any of our tracer population densities in our assumed halo models are exact representations of the satellites in the outer parts of the Milky Way, though Fig. 2 assures us that they are surely not grossly wrong. Modelling uncertainty could be minimised by the use of non-parametric fitting as advocated by Merritt and co-workers, although this would only be advantageous with a significantly larger dataset (see e.g., Merritt & Tremblay 1993).

The first major modelling uncertainty stems from our ignorance of the velocity anisotropy of the satellites, or equivalently the value of  $\beta$ . To investigate this, datasets are generated for known anisotropies and the Bayesian analysis is then applied assuming no knowledge of  $\beta$ . The histograms in Figs. 9 (a) and (b) show the spread in mass estimates obtained from samples of 30 data points with  $\beta > 0$  and  $\beta < 0$  both without and with proper motion data. Using only radial velocities, tangentially anisotropic ( $\beta < 0$ ) velocity distributions cause underestimates in the mass as the unknown tangential velocities of the satellites are, on average, greater than their known radial velocities. This effect is really a consequence of our assumed prior, which favours radial anisotropy. It is absent for radially anisotropic velocity distributions, as the broken curve in Fig. 11 (a) demonstrates. Fig. 11 (b) shows that the inclusion of proper motions removes this problem. Now, there is a mild tendency to overestimate the mass by at most  $\sim 30\%$  for the tangentially anisotropic case. On comparing the separation of the peaks in the distributions for  $\beta > 0$  and  $\beta < 0$  in Figs. 9 (a) and (b), we find that it is  $\sim 80\%$  of  $M$  when only radial velocities are used, and reduces to  $\sim 40\%$  of  $M$  when proper motion data are included. This is a typical measure of the error caused by uncertainty in the velocity distributions. We conclude that this is a serious source of uncertainty, though not as problematic as the measurement errors.

Fig. 11 (c) shows how the use of an incorrect halo model affects the mass estimate. The datasets used to produce

these histograms are generated according to a shadow tracer profile with  $a_s = 100$  kpc, but are assumed to be a power-law tracer population with  $\gamma = 4.0$  when applying the Bayesian analysis. It is clear from the comparative narrowness of the histograms in Fig. 11 (c) that the effects of this modelling uncertainty are less serious than problems caused by the measurement errors and the velocity anisotropy (as well as the small size of the dataset to be discussed in the next Section). For example, the standard deviation of the mass estimates in the case in which proper motions are included (the solid line in Fig. 11 (c)) is 15% of  $M$  and is thus much less than the intrinsic spread due to other causes. Only if our assumptions regarding the satellite number density are grossly incorrect can such modelling uncertainty be a grave problem. Serious incompleteness in the dataset might be a cause of such blundering. However, it does seem that our dataset can be missing at most only a few satellites. For example, Kleyna, Geller, Kenyon & Kurtz (1997) argue that the current sample is complete to the limits of current surveys. By extrapolating the luminosity function in the absence of a cut-off, they suggest that by surveying all the sky  $\sim 1.5$  magnitudes deeper, perhaps a further  $\sim 5$  dwarfs may be recovered.

As is evident from the work in Sections 3 and 4, the decision whether to fix the velocity normalisation or allow it to vary is another modelling uncertainty. Fig. 11 (d) shows the spread in mass estimates obtained from datasets of 30 points with radial velocities only, each dataset being generated for  $v_0 = 220 \text{ km s}^{-1}$  but being analysed with  $v_0$  as a free parameter. While the figure clearly shows a systematic underestimate of the mass, it is important to note that this effect is mainly due to the small size of the dataset. Comparison with the dashed curve in Fig. 12 (a), which presents the results from simulations in which  $v_0$  is assumed to be known, shows that the velocity normalisation uncertainty is dominated by the statistical noise in the case of 30 data points. We conclude that lack of knowledge of the velocity normalisation does not degrade our current mass estimate significantly, although it does affect our ability to estimate  $v_0$  and the scalelength  $a$  as individual parameters.

## 6 FUTURE PROSPECTS

The mass of the Milky Way is presently fixed by a dataset of 27 objects with known distances and radial velocities, of which 6 also possess measured proper motions. This is evidently a scanty dataset on which to base measurements of one of the most fundamental Galactic parameters. So, there is a pressing need for more data. What are the prospects for the future? Here, we consider the effects of forthcoming space missions in Section 6.1 and the new generation of large telescopes in Section 6.2.

### 6.1 The Astrometric Satellites

As the sample of satellite galaxies is nearly complete, the dataset can be extended only by measurements of their proper motions. Here, the outlook is good, with the *Space Interferometry Mission* (SIM) and the *Global Astrometry Interferometer for Astrophysics* (GAIA) satellites scheduled to obtain microarcsecond astrometry on objects brighter than

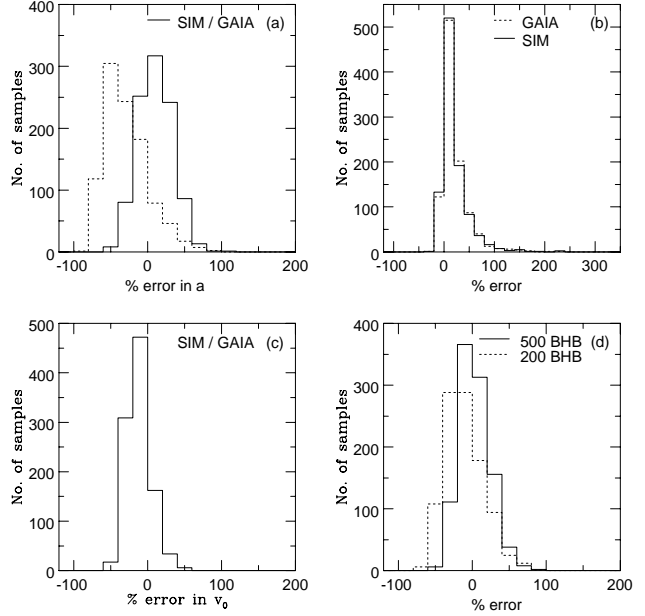


**Figure 12.** Histograms illustrating the impact of future developments on the determination of  $M$ . As in other figures, the histograms show how many out of 1000 datasets yielded a given percentage error in  $M$ . (a) 30 points with radial velocities only (dashed line) and with both radial velocities and proper motions (solid line) – as indicated, the latter case is how the dataset should look after the SIM and GAIA missions; (b) Comparison of the effects of measurement errors at the level of both GAIA (dashed line) and SIM (solid line); (c) Uncertainty in the velocity normalisation from datasets of 30 data points with radial velocities and proper motions; (d) 200 points (dashed line) and 500 points (solid line) with radial velocities only. Both these histograms assume a magnitude cut-off of  $m_v < 21.5$  and take account of the spread in intrinsic magnitudes of BHB stars. See text for discussion.

$V = 20$ . SIM is a pointing instrument and so will look at relatively few objects with great accuracy. GAIA is a scanning instrument with poorer accuracy but it will prove powerful for statistical analyses of larger samples. For SIM, wide angle astrometry is planned to yield proper motions accurate to  $\sim 2\mu\text{as yr}^{-1}$  for  $V = 20$  objects, though this requires long integration times of  $\gtrsim 4$  hours. As time on the instrument may well be at a premium, this may mean that SIM will examine only a limited number of faint objects and perhaps only some of the satellite companions of the Milky Way. The colour-magnitude diagrams of even the distant Leo I show the tip of the giant branch is still visible at  $V = 20$  (Caputo, Cassisi, Castellani & Marconi 1998; Hernandez-Doring, Valls-Gabaud & Gilmore 1999). So, even for Leo I, SIM can find the proper motions to  $\sim 5 \text{ km s}^{-1}$  by observing one or two stars (the internal velocity dispersion is of course much less than the systemic proper motion of the dwarf galaxy).

For GAIA, the target is  $10\mu\text{as yr}^{-1}$  in proper motion accuracy at  $V = 15$  and  $100 - 200\mu\text{as yr}^{-1}$  at  $V = 20$ . The poorer accuracy of GAIA means that the individual proper motions of bright stars at the distance of Leo I are still only accurate to  $\sim 240 \text{ km s}^{-1}$ . However, GAIA will measure the proper motions of all the stars brighter than  $V = 20$ , and therefore the proper motion of the satellite can be recovered

to good accuracy, as we now show. Caputo et al.'s (1998) colour-magnitude diagram is derived from three *Wide Field Planetary Camera* (WFPC2) frames with the aperture centered on Leo I. The field of view is  $\sim 1.7 \text{ arcmin}^2$ . There are  $\sim 50$  stars brighter than  $V = 20$  visible on the colour-magnitude diagram. Leo I subtends perhaps  $\sim 10 \text{ arcmin}^2$  on the sky, using the exponential radius given in Mateo (1998). In total, therefore, Leo I has perhaps  $\sim 290$  stars brighter than  $V = 20$ , and so the error on the proper motion of the ensemble is less by a factor of  $\sim 17$ . In other words, the components of the space motion of Leo I are obtainable to an accuracy of perhaps  $\sim 14 \text{ km s}^{-1}$  with GAIA. For closer satellites like Draco and Ursa Minor, the situation is even more favourable. Hernandez-Doring et al. (1999) provide a colour-magnitude diagram for Ursa Minor which has  $\sim 17$  stars brighter than  $V = 20$  and is derived from single chip WFPC2 observations. Each chip represents a field of view of  $0.6 \text{ arcmin}^2$ . Taking the exponential scalelength as  $8.0 \text{ arcmin}$  (Mateo 1998), then the number of stars in Ursa Minor brighter than  $V = 20$  is  $\sim 5700$ . So, GAIA can provide the components of the space motion of Ursa Minor to an accuracy of  $\sim 1 \text{ km s}^{-1}$ . To analyse the implications of SIM and GAIA, it is thus reasonable to assume that they can provide the space motions to better than 10%, though the distances of the objects may not be substantially improved.

Let us now investigate both the likely error caused by the small number of data points available, as well as future prospects from SIM and GAIA. We generate 1000 datasets with 30 data points, both for the case in which knowledge of only radial velocities is assumed and that in which the full space velocities are presumed to be measured by a combination of SIM and GAIA. The results are reported in Fig. 12. From Fig. 12 (a), we see that when the number of data points is 30, and only radial velocity data are used, the probability of obtaining an estimate of  $M$  which differs from the true value by more than a factor of two is about 30%. There is also evidence for a systematic underestimate in the mass when only radial velocities are used. This result is true whether or not the value of  $v_0$  is held fixed during the Bayesian analysis – this can be seen by comparing the dashed curve in Fig. 12 (a) with Fig. 11 (d). We note that this underestimate probably represents the worst case since the artificial data were generated from an isotropic model ( $\beta = 0$ ), but were analysed assuming the uniform energy prior on  $\beta$ . As noted previously, this prior is biased towards radial anisotropy. In the present case, this bias causes the Bayesian algorithm to systematically underestimate the kinetic energies of the satellites by assuming that most of their motion is contained in their observed radial velocities, which leads to a systematic underestimate of the total mass.

When we include tangential velocities, this systematic effect is removed and the probability of obtaining a mass estimate more than a factor of two different from the true value is reduced to just 2%. We conclude that SIM and GAIA have the potential to improve matters substantially by removing the bias to lower masses which is present if only radial velocities are available.

Fig. 12 (b) illustrates how the reduction of the proper motion errors will dramatically reduce the uncertainty due to measurement errors described in Section 5. To produce this figure, datasets of 30 data points with both radial velocities and proper motions were generated. Measurement

errors of  $100 \mu\text{as yr}^{-1}$  and  $2\mu\text{as yr}^{-1}$  were assumed for the GAIA and SIM missions respectively. In the case of GAIA, it is assumed that for each dwarf galaxy typically 400 stars brighter than  $V=20$  are observed, thereby reducing the error in the individual proper motions by a factor of 20. From Fig. 12 (b), we find that the spread in mass estimates due to measurement uncertainties for both GAIA and SIM is  $\sim 18\%$ , a huge improvement on the current situation (see Fig. 10 (a)). SIM and GAIA also have the potential to reduce the uncertainty in the velocity normalisation alluded to in Section 5. Fig. 12 (c) presents a histogram of velocity normalisation estimates from datasets of 30 data points with radial velocities and proper motions. The peak of the histogram lies within 20% of the true value and the mean absolute deviation is just 16%. Thus, after SIM and GAIA it will certainly be possible to assess whether the velocity normalisation of the halo is very different from  $220 \text{ km s}^{-1}$ .

Following the SIM and GAIA missions, all the major sources of error will have been reduced to below the levels of the statistical noise illustrated by the solid histogram of Fig. 12 (a). The average absolute deviation caused by the sparse dataset is  $\sim 20\%$  and this represents the best that can be achieved with the satellite galaxy dataset.

## 6.2 Blue Horizontal Branch Stars

The only option for substantially increasing the size of the dataset is to use distant spheroid stars, especially the comparatively bright blue horizontal branch (BHB) stars. For example, Warren and collaborators (1998, private communication) have begun a program of surveying selected fields in the Milky Way halo for BHB stars and plan to amass a dataset of  $\sim 200$  with accurate distances and radial velocities within the next few years. Miller (1998, private communication) reports that the 2df survey has discovered  $\sim 1000$  blue horizontal branch stars in a patch of the sky covering 750 square degrees. The present radial velocities are too crude to be of direct use in measuring the mass of the Milky Way halo. However, the dataset could be re-observed from the ground with the *Very Large Telescope* (VLT) to provide accurate radial velocities with only a modest investment of telescope time. The advantage of using stellar tracers of the distant halo is partly offset by complexity of modelling, as the selection effects have to be taken into account. In what follows, we modify the procedure of Section 2.3 to take account of two factors. First, the BHB stars have a distribution of absolute magnitudes, which we assume to be uniform in the range  $[M_{\min}, M_{\max}]$ . By studying the dataset of Flynn et al. (1995), it seems reasonable to take  $M_{\min} = 0.5$  and  $M_{\max} = 1.0$  for BHB stars. Second, we can only observe stars brighter than a certain magnitude threshold  $m_t$  (which we take to be  $m_t = 21.5$ , an optimistic estimate for the VLT). This means that the probabilities  $P(r, v_r | a, \beta)$  (from Table 1) are multiplied by the selection factor  $\epsilon(s)$

$$\epsilon(s) = \frac{m_t - 5 \log_{10} s - 10 - M_{\min}}{M_{\max} - M_{\min}} \quad s_{\min} < s < s_{\max} \quad (24)$$

Here,  $s$  is the heliocentric position in kpc, and we have defined

$$\begin{aligned} s_{\min} &= 10^{0.2(m_t - M_{\max} - 10)}, \\ s_{\max} &= 10^{0.2(m_t - M_{\min} - 10)}. \end{aligned} \quad (25)$$

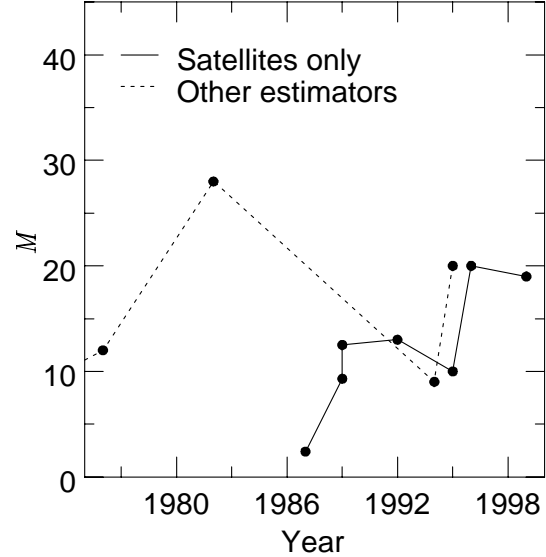
This selection factor (24) is unity when  $s < s_{\min}$  and vanishes when  $s > s_{\max}$ . Our procedure is to generate positions and velocities for the BHB stars from a power-law tracer whose density falls off like  $\sim r^{-3.5}$ . We then choose an absolute magnitude uniformly from our assumed uniform distribution of intrinsic magnitudes and test to see if this BHB star lies in the observable sample. In this way, simulated datasets of 200 and 500 BHB stars are generated and then analysed with the Bayesian algorithm, incorporating of course our new selection factor (24).

Fig. 12 (d) shows histograms for 1000 datasets of samples of 200 and 500 BHB stars. In both these histograms, it is clear that the systematic underestimate evident in Fig. 12 (a) is not present. Samples of such sizes are large enough to evade this awkward effect. However, a price is paid for using magnitude-limited samples, in that the histograms have somewhat larger spreads than the equivalent histograms for simulated data of complete samples. Nonetheless, with a dataset of 200 BHB radial velocities, the average absolute deviation about the mean mass estimate is just 21% and with 500 points it is 17%. These numbers clearly illustrate the value of using the BHB stars to augment the satellite dataset. BHB datasets will remove any possible problem with the systematic underestimate that is present in the much smaller satellite galaxy dataset. Measurement errors are less important than the statistical effect that comes from the bias in the sample introduced by the selection factor. It is this that causes the broadening of the dashed histogram in Fig. 12 (d). Assembling a dataset of  $\sim 200$  BHB stars with radial velocities and distances accurate to  $\sim 10\%$  is very clearly worth doing, as the investment of telescope time is not substantial compared to the scientific pay-off. The advantages of extending the BHB dataset to  $\sim 500$  stars appear to be slight – the average absolute error is reduced by only  $\sim 4\%$ , although the peak in the histogram is more centred on the true value.

## 7 CONCLUSIONS

This paper has presented a consistent estimate of the mass of the Milky Way. Previous analyses have given different answers depending on whether or not Leo I is included in the dataset. Our modelling has advanced the debate by providing a consistent answer irrespective of the presence or absence of Leo I, provided both the radial velocity and available proper motions are used. The consequent mass estimates and likelihood contours are in much better agreement than previously obtained. This happy circumstance is caused partly by the improved information on the proper motions of the dwarfs and partly by the new halo model. By generating simulated data, it is also straightforward to answer the question: How likely is it that, in a dataset of  $\sim 30$  satellites with known radial velocities, there is an object like Leo I whose inclusion or exclusion changes the inferred mass in a dramatic way (or, more specifically, by a factor of  $\sim 5$ )? This is actually not common, happening only some  $\sim 0.5\%$  of the time. Although prior expectation does not favour the existence of a Leo I, such a happenstance is not impossible (the probability is small, but not zero).

Our best estimate is a total mass of the Milky Way halo of  $\sim 1.9 \times 10^{12} M_{\odot}$  and a halo scalelength of  $\sim 170$  kpc. What is the likely error in this mass estimate? Using synthetic



**Figure 13.** Recent estimates of the total Mass of the Milky Way (in units of  $10^{11} M_{\odot}$ ). Those based on satellite motions only are shown by the solid line, while those based on other arguments (e.g. Local Group timing) are shown by the dotted line. Sources: Einasto, Haud, Joeveer & Kaasik (1976), Lin & Lynden-Bell (1982), Little & Tremaine (1987), Zaritsky, Olszewski, Schommer, Peterson & Aaronson (1989), Kulessa & Lynden-Bell (1992), Byrd, Valtonen, McCall & Innanen (1994), Lin, Jones & Klemola (1995), Peebles (1995), Kochanek (1996), this paper (1999)

datasets of radial velocities of 30 satellites, we have shown that there is a systematic tendency to underestimate the mass. The probability of obtaining a mass estimate which is smaller than the true value by more than a factor of two is  $\sim 30\%$ . From our analysis of the likely sources of error in Section 5, we conclude that – in addition to the systematic effect caused by the small size of the dataset – measurement errors are the most troublesome with the uncertainties in the proper motions being the main culprits. The net effect of these two main sources of error is a spread with a half-width of  $\sim 90\%$  coupled with a possible systematic underestimate of a factor of two. Taking this into account, our value for the mass of the Milky Way halo including the errors is  $\sim 1.9_{-1.9}^{+4.0} \times 10^{12} M_{\odot}$ . Fig. 13 shows a graph of recent mass estimates of the Milky Way halo based solely on the motions of the satellites and globular clusters (solid line), together with those based on other arguments (dotted line). Over the past 15 years, there has been a tendency for an increase in the mass estimates obtained from satellite radial velocities due to the increased size of the dataset and the availability of more proper motions. Our mass estimate is a slight decrease on the most recent previous determination by Kochanek (1996) and but it still fits into this general trend. We note that the mass estimates obtained from a variety of methods are now in good agreement. Zaritsky (1998) makes the point that the data from a variety of sources are consistent with an isothermal sphere of amplitude 180 – 220  $\text{km s}^{-1}$  extending outwards to  $\gtrsim 200$  kpc, a conclusion which agrees well with our results.

We have also explored the effects of allowing the normalisation  $v_0$  to vary as a free parameter. When the prior probability is  $1/v_0^2$  we obtain a most likely value of  $\sim 280$   $\text{km s}^{-1}$ , independent of the presence or absence of Leo I. The most likely values of  $a$  are 110 kpc when Leo I is included and 50 kpc when Leo I is excluded, leading to mass estimates of  $2.0 \times 10^{12} M_\odot$  and  $0.9 \times 10^{12} M_\odot$  respectively. This analysis also yields strongly tangential values for the velocity anisotropy  $\beta$ . However, all the results of the 3-parameter fitting exhibit a strong sensitivity to the choice of prior probabilities for  $v_0$  and  $\beta$  which suggests that they should not be given too much weight. We conclude that at present the small amount of data, crucially in the area of satellite proper motions, means that it is not feasible to constrain  $v_0$  with any degree of confidence.

The mass of the Milky Way halo within 50 kpc is  $\sim 5.4_{-3.6}^{+0.2} \times 10^{11} M_\odot$ . This is a more robust quantity than the total mass. Our error estimates are inferred from the maximum and minimum values of the total mass. Note that the errors on the mass within 50 kpc are asymmetrically distributed about the most likely value in the opposite sense to the errors in the total mass. This seems slightly counterintuitive. The reason is that increasing the total mass of the halo above  $\sim 1.9 \times 10^{12} M_\odot$  has little effect on the mass within 50 kpc, whereas diminishing the total mass can cause more significant changes. It is, of course, the mass within 50 kpc that is the relevant figure to bear in mind when considering interpretations of the microlensing experiments. For example, Honma & Kan-ya (1998) have argued that the Milky Way need not have a flat rotation curve out to 50 kpc and hence suggest that the timescales of the lensing events are consistent with brown dwarfs. The total mass in their Plummer model of the halo is just  $1.1 \times 10^{11} M_\odot$ . Though this may be consistent with the gas rotation curve (which cannot be traced beyond 20 kpc), it is quite incompatible with the mass estimates derived from the satellite galaxies (as well as the orbit of the Magellanic Stream). The origin of the microlensing events towards the Large Magellanic Cloud is presently unknown and a number of intriguing suggestions have been made. For example, they may lie in the Large Magellanic Cloud itself (Sahu 1994), or in an intervening stellar population or tidal shroud (Zaritsky & Lin 1997; Zhao 1998) or even in the warped and flaring Milky Way disk (Evans, Gyuk, Turner & Binney 1998). Nonetheless, Alcock et al. (1997) assert that the lenses largely lie in the Milky Way halo and provide a model-independent estimate of the halo mass in the lensing population within 50 kpc of  $2.0_{-0.7}^{+1.2} \times 10^{11} M_\odot$ . If their assumption as to the location of the lenses is correct, the microlensing results imply that  $\sim 36\%$  of the halo within 50 kpc is baryonic with the remainder of the halo being built from elementary particles or baryonic objects (such as cold molecular clouds) that do not produce microlensing. However, as can be deduced from the error bounds, the baryonic fraction is not well constrained at the moment.

Current estimates of the total mass of the Local Group set it at  $\sim 4 - 8 \times 10^{12} M_\odot$  (e.g., Peebles 1996, Schmoldt & Saha 1998). Based on their asymptotic rotation curves, M31 is  $\sim 30\%$  more massive than the Milky Way. Given our result for the Milky Way halo, this implies that the mass of M31 is  $\sim 3.0 \times 10^{12} M_\odot$ . We conclude that more than 50% (and perhaps almost all) of the mass in the Local Group is

concentrated around the two largest group members. Let us note that these results receive confirmation from recent work of Peebles using his numerical action method. For example, Peebles (1995, 1996) obtains a mass for the Milky Way halo of  $\sim 2 \times 10^{12} M_\odot$  and a mass for M31 of  $\sim 3.4 \times 10^{12} M_\odot$  using the motions of the most distant Local Group satellites.

The coming decade promises to be fruitful in terms of the availability of new data. We have shown that obtaining radial velocities for large samples of blue horizontal branch stars can provide a very promising line of attack on the problem. A dataset of even 200 such stars will reduce the statistical uncertainty in the mass estimate to  $\sim 21\%$ , as well as removing the possible systematic effect that occurs with the small samples of satellite galaxies. This illustrates that the scientific returns from such a program could be high for a relatively low investment of telescope time. In the longer term, SIM and GAIA will be able to measure the proper motions of all the Milky Way satellites. For example, using the colour-magnitude diagrams, we have shown that the proper motions of the most distant dwarfs like Leo I will be determined to  $\sim 5 - 14 \text{ km s}^{-1}$ , while the nearer dwarfs like Ursa Minor will be determined to  $\sim 1 \text{ km s}^{-1}$ . This will provide the mass of the Milky Way halo to within  $\sim 20\%$  and will also allow the amplitude of the velocity normalisation to be determined to within  $\sim 16\%$ .

It has been suggested by Johnston et al. (1998) that SIM and GAIA may be used to measure the proper motions of stars in a stream and hence to find the mass of the Milky Way halo. In particular, they suggest that measuring the proper motions of 100 stars brighter than 20th magnitude in a tidal stream to  $\sim 4 \mu\text{as yr}^{-1}$  may be enough to determine the mass of the Milky Way to a few percent. Such an accuracy on the proper motions is not achievable at  $V = 20$  for GAIA. For SIM, wide angle astrometry to this accuracy requires long integration times of  $\gtrsim 4$  hours. The mass of the Milky Way within 50 kpc is reasonably certain, and it is data collected on objects beyond 50 kpc (and preferably beyond 100 kpc) that is most helpful in discriminating between models (see, for example, Fig. A1 of Lynden-Bell & Lynden-Bell 1995). Unfortunately, there is no known stellar stream at such large Galactocentric radii for use as a SIM target. At large distances, the proper motion errors of individual stars will remain large with available technology, thus frustrating any certain identification of stream candidates. It is also important to assess the effects of some of the assumptions made by Johnston et al. (1998) before the figure of a few percent error can be accepted, as it does not include all the modelling and measurement errors.

As data beyond 50 kpc is scarce, we believe that the optimal approach is to use every scrap of information. We believe that the future will belong to joint analyses of the datasets of both the radial and proper motions of the satellites together with large samples of distant BHB stars. This is the best strategy for reducing both the statistical noise and the measurement uncertainties.

## ACKNOWLEDGMENTS

NWE thanks the Royal Society for financial support, while MIW acknowledges help from a Scatcherd Scholarship. We thank Geza Gyuk, Xavier Hernandez-Doring, Paul Hewett,

Eamonn Kerins, Mike Irwin, Jenny Read, David Valls-Gabaud and Steve Warren for helpful discussions and suggestions. Gerry Gilmore, Michael Perryman and Tim de Zeeuw provided useful information on the GAIA satellite. We also thank the referee, Scott Tremaine, for several insightful comments on this work.

## REFERENCES

Alcock C. et al., 1997, *ApJ*, 486, 697  
 Binney J., Tremaine S., 1987, *Galactic Dynamics*, Princeton University Press, Princeton  
 Byrd G., Valtonen M., McCall M., Innanen K., 1994, *AJ*, 107, 2055  
 Caputo F., Cassisi S., Castellani M., Marconi G., 1998, *astro-ph/9812266*  
 Cowsik R., Ratnam C., Bhattacharjee P., 1996, *Phys. Rev. Lett.*, 76, 3886  
 Dauphole B., Geffert M., Colin J., Ducourant C., Odenkirchen M., Tucholke H.-J., 1996, *A&A*, 313, 119  
 Dejonghe H., 1986, *Phys. Rept.*, 133, 217  
 Dubinski J., Carlberg R., 1991, *ApJ*, 378, 496  
 Eddington A. S., 1916, *MNRAS*, 76, 572  
 Einasto J., Haud U., Joeveer M., Kaasik A., 1976, *MNRAS*, 177, 357  
 Evans N.W., 1994, *MNRAS*, 267, 333  
 Evans N.W., 1997, *Phys. Rev. Lett.*, 78, 2260  
 Evans N.W., Gyuk G., Turner M.S., Binney J.J., 1998, *ApJ*, 501, L45  
 Evans N.W., Häfner R.M., de Zeeuw P.T., 1997, *MNRAS*, 286, 315  
 Fich M., Tremaine S.D., 1991, *ARA&A*, 29, 409  
 Flynn C., Sommer-Larsen J., Christensen P.R., Hawkins M.S.R., 1995, *A&ASS*, 109, 171  
 Fusi Pecci F., Bellazzini M., Cacciari C., Ferraro F. R., 1995, *AJ*, 110, 1664  
 Gates E., Kamionkowski M., Turner M.S., 1997, *Phys. Rev. Lett.*, 78, 2261  
 Harris W. E., 1996, *AJ*, 112, 1487  
 Hénon M., 1973, *A&A*, 24, 229  
 Hernandez-Doring X., Valls-Gabaud D., Gilmore G., 1999, *MNRAS*, submitted  
 Hernquist L., 1990, *ApJ*, 356, 359  
 Honma M., Kan-ya Y., 1998, *ApJ*, 503, L139  
 Jaffe W., 1983, *MNRAS*, 202, 995  
 Jeans J.H., 1919, *Phil. Trans. Roy. Soc. London A*, 218, 157  
 Johnston K.V., Zhao H.S., Spergel D.N., Hernquist L., 1999, *ApJ*, 512, L109  
 Kendall M., Stuart A., 1977, *The Advanced Theory of Statistics*, Griffin, London  
 Kleyna J.T., Geller M.J., Kenyon S.J., Kurtz M.J., 1997, *AJ*, 113, 624  
 Kochanek C., 1996, *ApJ*, 457, 228  
 Kroupa P., Bastian U., 1997, *New Astronomy*, 2, 77  
 Kulessa A.S., Lynden-Bell D., 1992, *MNRAS*, 255, 105  
 Kunkel W.E., Demers S., 1976, *Greenwich Obs. Bull.*, 182, 241  
 Lin D.N.C., Jones B.F., Klemola A.R., 1995, *ApJ*, 439, 652  
 Lin D.N.C., Lynden-Bell D., 1982, *MNRAS*, 198, 707  
 Lindegren L., Perryman M.A.C., 1996, *A&AS*, 116, 57  
 Little B., Tremaine S.D., 1987, *ApJ*, 320, 493  
 Lynden-Bell D., 1976, *MNRAS*, 174, 695  
 Lynden-Bell D., Frenk C., 1981, *Observatory*, 101, 200  
 Lynden-Bell D., Lynden-Bell R., 1995, *MNRAS*, 275, 429  
 Majewski S. R. & Cudworth K. M., 1993, *PASP*, 105, 987  
 Mateo M., 1998, *ARA&A*, 36, 435  
 Merritt D., Tremblay B., 1993, *AJ*, 106, 2229

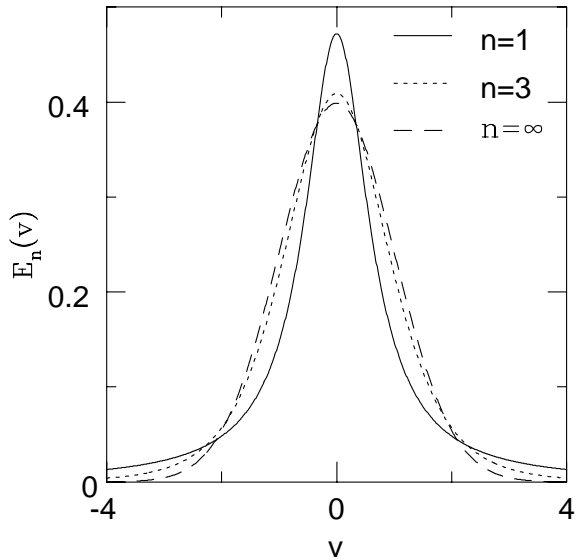


**Figure A1.** Comparison between three members of the  $E_{L,n}$  family of error convolution functions, showing rapid convergence to a Gaussian distribution ( $n = \infty$ ).

**Table A1.** Table giving  $\sigma_n$  in terms of  $\sigma_G$  for a range of values of  $n$ .

$n$	$\sigma_n$
1	0.4769 $\sigma_G$
2	0.7637 $\sigma_G$
3	0.8473 $\sigma_G$
4	0.8872 $\sigma_G$
5	0.9106 $\sigma_G$
10	0.9561 $\sigma_G$
20	0.9782 $\sigma_G$

Odenkirchen M., Brosche P., Geffert M., Tucholke, H-J., 1997, *New Astronomy*, 2, 477  
 Peebles P. J. E., 1995, *ApJ*, 449, 52  
 Peebles P. J. E., 1996, in "Gravitational Dynamics", Cambridge University Press, eds. Lahav O., Terlevich E., Terlevich R. J., p219  
 Press W.H., Teukolsky S.A., Vetterling W.T., Flannery B.P., 1992, *Numerical Recipes*, chap. 14, Cambridge University Press, Cambridge  
 Pryor C., 1998, in "Proceedings of the Rutgers Conference on Galaxy Dynamics", ed. Sellwood, J.A.  
 Sahu K., 1994, *Nature*, 370, 275  
 Schmoldt I., Saha P., 1998, *AJ*, 115, 2231  
 Scholz R.-D., Irwin M.J., 1994, *IAU*, 161, 535  
 Schweitzer A.E., Cudworth K.M., Majewski S.R., Suntzeff N.B., 1995, *AJ*, 110, 2747  
 Schweitzer A.E., Cudworth K.M., Majewski S.R., 1997, *PASP*, 127, 103  
 Summers D., Thorne R. M., 1991, *Phys. Fluids B*, 3, 1835  
 Unwin S., Boden A., Shao M. 1997, *Proc. STAIF*, AIP Conference Proceedings 387, 63  
 Vasyliunas V. M. 1968, *J. Geophys. Res.*, 73, 2839  
 Zaritsky D., 1998, in "The Third Stromlo Symposium", ASP Conf. Series, Vol. 165, 34  
 Zaritsky D., Lin D.N.C., 1997, *AJ*, 114, 2545  
 Zaritsky D., Olszewski E.W., Schommer R.A., Peterson R.C., Aaronson M. 1989, *ApJ*, 345, 759

Zhao H.S. 1996, MNRAS, 278, 488  
 Zhao H.S. 1998, MNRAS, 294, 139

## APPENDIX A: A FAMILY OF ERROR CONVOLUTION FUNCTIONS

In this appendix, we present the properties of a family of error convolution functions which we call the generalised Lorentzian family. These functions are already known in the plasma physics literature (Vasyliunas 1968, Summers & Thorne 1991), but do not seem to be readily available in the astronomical literature. The  $n$ th member of this family  $E_n$  is given by

$$E_n(v) = \frac{1}{\sqrt{2\pi}n\sigma_{L,n}} \frac{\Gamma[n]}{\Gamma[n-1/2]} \frac{(2n\sigma_n^2)^n}{(2n\sigma_n^2 + v^2)^n}. \quad (\text{A1})$$

The  $n = 1$  member is the Lorentzian  $E_1$  which we use in our calculations to take account of the observational errors in the proper motions of the satellites. In the limit  $n \rightarrow \infty$ , the error convolution function becomes

$$E_\infty(v) = \frac{1}{\sqrt{2\pi}\sigma} e^{\frac{v^2}{2\sigma^2}}, \quad (\text{A2})$$

which is the familiar Gaussian. The convergence to a Gaussian is very rapid with increasing  $n$  and, as Fig. A1 shows,  $E_3$  is already a close approximation to a Gaussian, although it remains somewhat broader.

To normalise the  $E_n$  family, we demand that the quartiles for each member be the same as those of a Gaussian of width  $\sigma_G$ . For a Gaussian, the quartiles  $x_G$  are given by solving

$$\text{Erf}\left[\frac{x_G}{\sqrt{2}\sigma_G}\right] = \frac{2}{\sqrt{\pi}} \int_0^{x_G/(\sqrt{2}\sigma_G)} e^{-t^2} dt = \frac{1}{2}. \quad (\text{A3})$$

Hence, we find that  $x_G = 0.67449\sigma_G$ . To find the corresponding value of  $\sigma_n$ , we must solve the integral equation

$$\frac{1}{\sqrt{2\pi}n\sigma_{L,n}} \frac{\Gamma[n]}{\Gamma[n-1/2]} \int_{-x_G}^{x_G} dv \frac{(2n\sigma_n^2)^n}{(2n\sigma_n^2 + v^2)^n} = \frac{1}{2}, \quad (\text{A4})$$

to obtain  $\sigma_n$  in terms of  $x_G$  (and hence in terms of  $\sigma_G$ ). This is analytically tractable only for  $n = 1$ , when we obtain  $\sigma_1 = 0.4769\sigma_G$ . For all other values of  $n$ ,  $\sigma_n$  must be found numerically. Some numerical values are presented for convenience in Table B1.

This paper has been produced using the Royal Astronomical Society/Blackwell Science TeX macros.